

1    **Dust storms from the Taklamakan Desert significantly darken snow**  
2    **surface on surrounding mountains**

3    Yuxuan Xing<sup>1</sup>, Yang Chen<sup>1</sup>, Shirui Yan<sup>1</sup>, Xiaoyi Cao<sup>1</sup>, Yong Zhou<sup>2</sup>, Xueying Zhang<sup>2</sup>,  
4    Tenglong Shi<sup>3</sup>, Xiaoying Niu<sup>1</sup>, Dongyou Wu<sup>1</sup>, Jiecan Cui<sup>4</sup>, Yue Zhou<sup>1</sup>, Xin Wang<sup>1</sup>,  
5    Wei Pu<sup>1</sup>

6    <sup>1</sup>Key Laboratory for Semi-Arid Climate Change of the Ministry of Education, College of Atmospheric  
7    Sciences, Lanzhou University, Lanzhou 730000, China

8    <sup>2</sup>Aviation University of Air Force, Changchun 130022, China

9    <sup>3</sup>Henan Industrial Technology Academy of Spatial-Temporal Big Data, Henan University, Kaifeng  
10   475004, China

11   <sup>4</sup>Zhejiang Development & Planning Institute, Hangzhou 310030, China

12   *Correspondence to:* Wei Pu (puwei@lzu.edu.cn)

13

14 **Abstract**

15 The Taklamakan Desert (TD) is a major source of mineral dust emissions into the  
16 atmosphere. These dust particles have the ability to darken the surface of snow on the  
17 surrounding high mountains after deposition, significantly impacting the regional  
18 radiation balance. However, previous field measurements have been unable to capture  
19 the effects of severe dust storms accurately, and their representation on regional scales  
20 has been inadequate. In this study, we propose a modified remote-sensing approach that  
21 combines data from the Moderate Resolution Imaging Spectroradiometer (MODIS)  
22 satellite and simulations from the Snow, Ice, and Aerosol Radiative (SNICAR) model.  
23 This approach allows us to detect and analyze the substantial snow darkening resulting  
24 from dust storm deposition. We focus on three typical dust events originating from the  
25 Taklamakan Desert and observe significant snow darkening over an area of  $\sim 2160$ ,  
26  $\sim 610$ , and  $\sim 640 \text{ km}^2$  in the Tien Shan, Kunlun, and Qilian Mountains, respectively. Our  
27 findings reveal that the impact of dust storms extends beyond the local high mountains,  
28 reaching mountains located approximately 1000 km away from the source. Furthermore,  
29 we observe that dust storms not only darken the snowpack during the spring but also in  
30 the summer and autumn seasons, leading to increased absorption of solar radiation.  
31 Specifically, the snow albedo reduction (radiative forcing) triggered by severe dust  
32 depositions is up to  $0.028\text{--}0.079$  ( $11\text{--}31.5 \text{ W m}^{-2}$ ),  $0.088\text{--}0.136$  ( $31\text{--}49 \text{ W m}^{-2}$ ), and  
33  $0.092\text{--}0.153$  ( $22\text{--}38 \text{ W m}^{-2}$ ) across the Tien Shan, Kunlun, and Qilian Mountains,  
34 respectively. This further contributes to the aging of the snow, as evidenced by the  
35 growth of snow grain size. Comparatively, the impact of persistent but relatively slow  
36 dust deposition over several months during non-event periods is significantly lower  
37 than that of individual dust event. This highlights the necessity of giving more attention  
38 to the influence of extreme events on the regional radiation balance. From this study,  
39 we gain a deeper understanding of how a single dust event can affect the extensive  
40 snowpack and demonstrates the potential of employing satellite remote-sensing to  
41 monitor large-scale snow darkening.

42 **1 Introduction**

43 High Mountain Asia (HMA), which includes the Tibetan Plateau (TP) and surrounding  
44 mountain ranges, holds the largest amount of glaciers and snow outside of the poles.  
45 This region is informally known as the “The Third Pole” and the “Asian Water Tower”  
46 (Yao et al., 2012, 2019) because of its extreme importance as a freshwater source, with  
47 approximately one billion people relying on the water and hydropower that the glaciers  
48 and snow across HMA regularly provide (Immerzeel et al., 2012; Mishra et al., 2018).  
49 The snow-covered area of HMA is a highly reflective natural surface that has a  
50 significant impact on the regional radiation balance (Cohen and Rind, 1991; Painter et  
51 al., 2012). Previous satellite and ground-based observations have demonstrated that the  
52 mass and extent of the snow cover across HMA are rapidly declining owing to recent  
53 global warming (Bormann et al., 2018; Notarnicola et al., 2020; Pulliainen et al., 2020).  
54 Furthermore, growing evidence has indicated that light-absorbing particles (LAPs)  
55 (Arun et al., 2019, 2021a, 2021b; Chaubey et al., 2010; Gogoi et al., 2018, 2021a; 2021b;  
56 Thakur et al., 2021), such as mineral dust and black carbon (BC), can induce snow  
57 darkening effect when they are deposited on the snow surface (Wang et al., 2013; Qian  
58 et al., 2015; Dang et al., 2017; Huang et al., 2022; Niu et al., 2022; Réveillet et al., 2022  
59 Shi et al., 2022c). This snow darkening effect increases solar absorption and decreases  
60 snow albedo, resulting in enhanced snowmelt (Hadley and Kirchstetter, 2012; Dumont  
61 et al., 2014; He et al., 2017, 2018; Pu et al., 2017; Shi et al., 2021, 2022a, 2022b;  
62 Cordero et al., 2022) and an accelerated transformation of ice and snow into liquid  
63 water in the Asian Water Tower (Yao et al., 2022). Consequently, the snow-darkening  
64 effect plays a critical role in snow decline across HMA, thereby perturbing the climate  
65 system and impacting hydrological cycles (Kraaijenbrink et al., 2017, 2021; Sang et al.,  
66 2019; Shi et al., 2019; Zhang et al., 2020, 2021; Roychoudhury et al., 2022; Yang et al.,  
67 2022).  
68 The Taklamakan Desert (TD) in southwestern Xinjiang, Northwest China, is the  
69 second-largest shifting sand desert on Earth and accounts for 42% of all dust emissions  
70 in East Asia (Chen et al., 2017a). Approximately 70.54 Tg of dust are emitted into the  
71 atmosphere annually, with the most intense dust events occurring in spring (Chen et al.,  
72 2017a). The dust in the Tarim Basin is predominantly redeposited onto nearby regions

73 owing to the surrounding high mountains (Qiu et al., 2001; Sun et al., 2001; Shao and  
74 Dong, 2006). When the dust is uplifted above 4 km altitude, it may eventually settle on  
75 the snow surfaces across the surrounding high mountains, such as the Tien Shan and  
76 Kunlun Mountains and subsequently induce a snow-darkening effect (Ge et al., 2014;  
77 Jia et al., 2015; Yuan et al., 2018). Furthermore, this dust is also transported eastward  
78 beyond the Tarim Basin and can be transported all the way to the Qilian Mountains via  
79 the westerly winds during spring and summer, thereby inducing a snow darkening effect  
80 in this distal region to the east of the TD (Dong et al., 2020; Han et al., 2022). Therefore,  
81 TD dust may have a profound effect on the regional radiative balance by darkening the  
82 snow across the high mountains surrounding the TD. This effect may subsequently  
83 accelerate snow melting and affect water resources for the 30+ million people living in  
84 the Xinjiang and Gansu provinces of China (Mishra et al., 2021).

85 Numerous field measurements have been undertaken in recent decades to investigate  
86 the dust content of snow/glaciers across the high mountains surrounding the TD, with  
87 measured dust contents generally varying from 1.4 to 110  $\mu\text{g g}^{-1}$  (Wake et al., 1994;  
88 Dong et al., 2009, 2014; Wu et al., 2010; Ming et al., 2016; Xu et al., 2016; Schmale et  
89 al., 2017; Zhang et al., 2018, 2021; Wang et al., 2019; Li et al., 2021, 2022). This  
90 abundance of dust particles has been found to induce a significant snow darkening  
91 effect across the high-mountain snowpack, thereby increasing its associated radiative  
92 forcing to 25.8–65.7  $\text{W m}^{-2}$ . Furthermore, the estimated natural dust-induced snow-  
93 darkening effect can be equivalent to that induced by BC, particularly during intense  
94 springtime dust events (Sarangi et al., 2020; Zhang et al., 2021). These findings  
95 effectively highlight the significance of the TD dust-induced snow darkening effect  
96 across the surrounding high mountains. In spite of these invaluable in situ findings,  
97 ground-based observations are poorly represented at the regional scale owing to limited  
98 spatial coverage and temporal discontinuity (Arun et al., 2019). Furthermore, these  
99 previous field measurements may not be able to capture severe dust emission and  
100 loading events, which are more likely to induce snow darkening than common dry and  
101 wet deposition processes (Dumont et al., 2020; Pu et al., 2021; Baladima et al., 2022).

102 Satellite remote sensing offers an effective way to overcome the limitations of ground-  
103 based measurements by providing a more comprehensive understanding of the LAP-  
104 induced impact on the regional radiative forcing of the snowpack (Skiles et al., 2018a).  
105 For example, Painter et al. (2012) found that the instantaneous LAP-induced radiative  
106 forcing can exceed  $250 \text{ W m}^{-2}$  in the Hindu Kush-Himalaya region via an analysis of  
107 Moderate Resolution Imaging Spectroradiometer (MODIS) satellite data. Sarangi et al.  
108 (2020) further revealed that dust is the primary factor responsible for high-altitude snow  
109 darkening in the Hindu Kush–Himalaya region. Similarly, severe dust events from the  
110 Sahara can deposit dust on the snowpack across the European Alps and Caucasus  
111 Mountains (Di Mauro et al., 2015; Dumont et al., 2020), with this deposition inducing  
112 a radiative forcing of up to  $153 \text{ W m}^{-2}$  based on satellite retrievals in Europe. Dust  
113 deposition has also induced extensive snow darkening across the Upper Colorado River  
114 Basin in North America, particularly during extreme dust events (Skiles et al., 2016,  
115 2018b; Painter et al., 2017). These studies have demonstrated the effectiveness of  
116 employing satellite remote sensing to estimate the dust content of the snowpack and its  
117 associated radiative forcing. However, detecting natural dust deposition on the snow  
118 surfaces across high mountains surrounding the TD is still limited.

119 Here we investigate the impact of dust storms on snow albedo reduction and radiative  
120 forcing across the high mountains surrounding the TD. We first capture three typical  
121 dust events that induced snow darkening in the Tien Shan, Kunlun, and Qilian  
122 Mountains, respectively. We then utilize MODIS satellite data and the Snow, Ice, and  
123 Aerosol Radiative (SNICAR) model to retrieve the dust content of the snowpack. We  
124 then capture three typical dust events that induced snow darkening in the Tien Shan,  
125 Kunlun, and Qilian Mountains, respectively. Finally, we analyze the spatial and  
126 altitudinal variations in dust-induced snow darkening and compare our retrievals with  
127 field measurements. Through remote sensing observations, we aim to provide a new  
128 view of the darkening effect of natural desert dust on the snowpack of the high  
129 mountains surrounding the TD.

130 **2 Methodology**

131 **2.1 Remote-sensing data**

132 We accessed two MODIS datasets, the surface reflectance (MOD09GA:  
133 <https://earthdata.nasa.gov>;  $500 \times 500$  m resolution) and aerosol optical depth (AOD;  
134 MCD19A2), to evaluate the impact of dust on snow albedo. MOD09GA is the daily  
135 surface reflectance product after the atmospheric correction from the Terra satellite,  
136 which provides the reflectance data for seven bands (band 1, 620–670 nm; band 2, 841–  
137 876 nm; band 3, 459–479 nm; band 4, 545–565 nm; band 5, 1230–1250 nm; band 6,  
138 1628–1652 nm; band 7, 2105–2155 nm). Previous studies have indicated that the  
139 MODIS sensor on Terra is not affected by saturation on bright snow surfaces. As a result,  
140 it has the capability of detecting changes in reflectance in the visible (VIS) bands caused  
141 by dust in snow (Painter et al., 2012; Pu et al., 2019). Additionally, we used the updated  
142 MODIS Aerosol Optical Depth (AOD) product MCD19A2, based on the MAIAC  
143 algorithm, to assess the AOD levels during dust events. This is a combined product of  
144 Terra/Aqua with a spatial-temporal resolution of 1km, which were resampled to 500m  
145 resolution using GEE (<https://earthengine.google.com>).

146 The daily averaged downward shortwave flux was obtained from the NASA Clouds  
147 and the Earth's Radiant Energy System (CERES: <https://ceres.larc.nasa.gov>;  $1^\circ \times 1^\circ$   
148 resolution). The CERES data products take advantage of the synergy between  
149 collocated CERES instruments and spectral imagers, such as MODIS (Terra and Aqua)  
150 and the Visual Infrared Imaging Radiometer Suite (S-NPP and NOAA-20). We used the  
151 downward shortwave flux to estimate the daily averaged radiative forcing that was due  
152 to dust deposition on the snowpack. The Cloud-Aerosol Lidar with Orthogonal  
153 Polarization (CALIOP/CALIPSO) provided by NASA is able to detect the type and  
154 height of aerosols in the atmosphere (Huang et al., 2007; Han et al., 2022) and can  
155 therefore be used to identify the movement of dust storms over the high mountains  
156 surrounding the TD.

157 The Shuttle Radar Topography Mission (SRTM) digital elevation data, which possess  
158 a 90-m spatial resolution, were provided by NASA and downloaded from Google Earth  
159 Engine (<https://earthengine.google.com>). These data were used to correct the influence  
160 of topography on surface reflectance.

161 **2.2 Snow depth and wind data**

162 The snow depth data were provided by NASA and accessed from the Modern-Era  
163 Retrospective Analysis for Research and Applications, Version 2 (MERRA-2:  
164 <https://gmao.gsfc.nasa.gov>). The MERRA-2 snow depth product was selected because  
165 it has better accuracy than those from ERA-Interim, JJA-55, and ERA5 across HMA  
166 (Orsolini et al, 2019). The wind field data were obtained from the European Centre for  
167 Medium-Range Weather Forecasts (ECMWF) Reanalysis v5 (ERA5:  
168 <https://www.ecmwf.int>) owing to its superior performance in terms of its high spatial  
169 resolution and longer time span compared with other products (Copernicus Climate  
170 Change Service, 2017). Here, we used ERA5 wind data at 700 hPa to describe the  
171 atmospheric circulation during the analyzed dust storms.

172 **2.3 Radiative-transfer model**

173 The SNICAR model is a two-stream radiative transfer model (Flanner et al., 2007, 2009)  
174 that has been widely used to simulate the spectral albedo of LAP-contaminated snow  
175 (Sarangi et al., 2019; Chen et al., 2021). The model includes snow properties such as  
176 snow depth and effective radius and accounts for the incident radiation at the surface  
177 and its spectral distribution, solar zenith angle, and the type and concentration of LAPs  
178 in the snowpack. In this study, dust optical parameters are taken from SNICAR defaults,  
179 where the refractive index is  $1.56 + 0.0038i$  at  $0.63 \mu\text{m}$  (Patterson et al., 1981; Flanner  
180 et al., 2007). And a diameter bin of  $0.1\text{-}1 \mu\text{m}$  was selected according to the previous  
181 observations from Taklamakan Desert (Okada and Kai, 2004). Furthermore, a single-  
182 layer snowpack model was adopted in our study, in line with Cui et al. (2021), since the  
183 snow darkening effect typically pertains to surface snow. This simplification minimally  
184 affects the retrieval of LAPs from the surface snow, despite the complex multilayer  
185 structure of natural snowpacks.

186 The Santa Barbara DISORT Atmospheric Radiative Transfer (SBDART) model is one  
187 of the most widely used models for simulating the surface solar irradiance in clear and  
188 cloudy sky conditions (Ricchiazzi et al., 1998). The SBDART model includes standard  
189 atmospheric models, cloud models, extraterrestrial source spectra, gas absorption  
190 models, standard aerosol models, and surface models. Here, we used the SBDART

191 model to calculate the spectral surface solar irradiance, following the approach of Cui  
192 et al. (2021). In this study, the cloud-free condition was set in SBDART, according to  
193 the MODIS images.

#### 194 **2.4 Terrain correction**

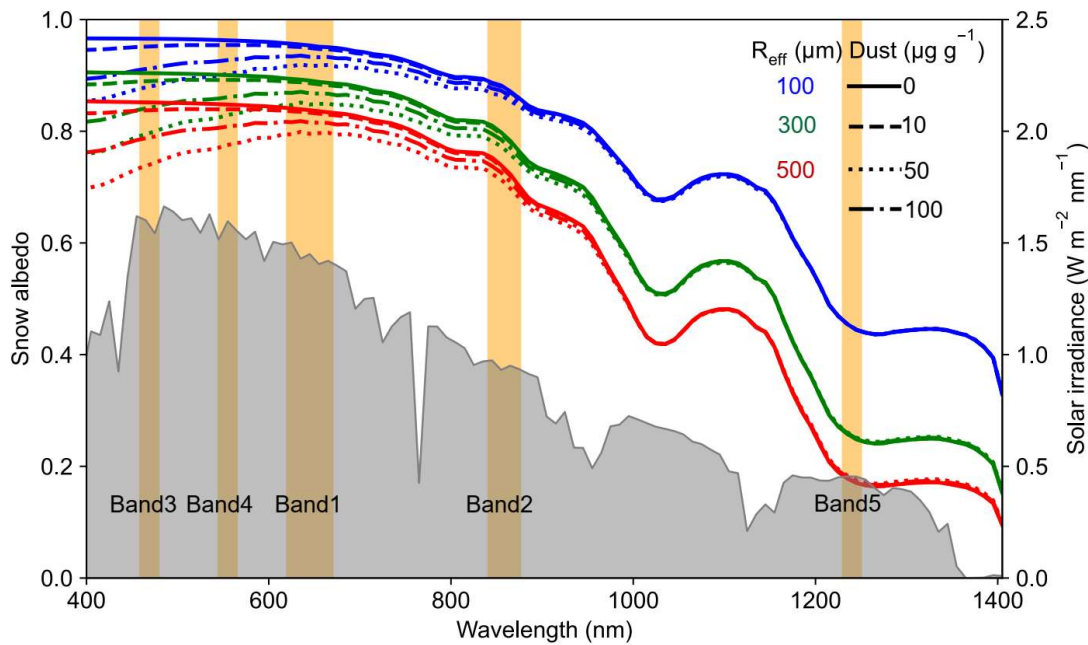
195 The high mountains surrounding the TD have a complex terrain, such that the local  
196 solar zenith angle ( $\beta$ ) may differ from the MODIS-derived solar zenith angle ( $\theta_0$ ).  
197 Therefore, the topographic correction method should be used to derive  $\beta$  (Teillet et al.,  
198 1982; Negi and Kokhanovsky, 2011):

199 
$$\cos \beta = \cos \theta_0 \cos \theta_T + \sin \theta_0 \sin \theta_T \cos (\phi_0 - \phi_T), \quad (1)$$

200 where  $\phi_0$  is the solar azimuth angle from MODIS, and  $\theta_T$  and  $\phi_T$  are the surface  
201 slope and aspect from SRTM, respectively. We then replace  $\theta_0$  with  $\beta$  in subsequent  
202 satellite retrievals.

#### 203 **2.5 Snow properties retrieval**

204 The dust-contaminated spectral snow albedo is determined based on the dust content,  
205 snow grain size, snow depth, and solar zenith angle (Wiscombe and Warren, 1980). The  
206 dust content and snow depth primarily impact the snow albedo in the ultraviolet (UV)  
207 and VIS wavelengths, with a much smaller effect on snow albedo in the near infrared  
208 (NIR) wavelengths (Figure 1 and Figure S1). Conversely, the snow grain size and solar  
209 zenith angle primarily impact the snow albedo in the NIR wavelengths. The solar zenith  
210 angle and snow depth data are from MODIS Terra and MERRA-2, respectively. We  
211 used the SNICAR model to derive the quantitative snow grain size and dust content  
212 from the MODIS data. Then the SBDART model was combined to estimate the dust-  
213 induced snow albedo reduction and radiative forcing. Figure 2 shows the flowchart of  
214 the overall retrieval process.



215

216 **Figure 1. Snow albedo spectra for different snow optical effective radius ( $R_{\text{eff}}$ ) and**  
 217 **dust contents that were simulated using the SNICAR model. Orange bars denote**  
 218 **MODIS bands, and the gray region represents the typical solar irradiance in HMA.**

219 The Snow-Covered Area and Grain size (SCAG) model is a spectral unmixing method  
 220 that is widely used for identifying snow cover fraction (SCF) and snow optical effective  
 221 radius ( $R_{\text{eff}}$ ), especially in complex mountain terrains (Painter et al., 2009, 2012; Rittger  
 222 et al., 2013). The SCAG model retrieves the SCF and  $R_{\text{eff}}$  using all seven bands of the  
 223 MODIS reflectance data, which span the VIS to NIR range. It does not consider the  
 224 impact of LAPs. However, in our study, the dust content in snow is extreme high, which  
 225 will significantly reduce the VIS snow albedo in MODIS bands 1, 3, 4 (Figure 1). So,  
 226 the SCAG model will introduce a large bias in the resultant SCF and  $R_{\text{eff}}$  retrievals.  
 227 Furthermore, the reflectance of fine-grained dirty snow has been compared with that of  
 228 pure coarse-grained snow at short-wave infrared wavelengths, which include bands 6  
 229 and 7 (Bair et al., 2020). The extremely high dust content in this study therefore means  
 230 that the reflectance in MODIS bands 6 and 7 is not appropriate for snow property  
 231 retrieval. Instead, we used the reflectance data in MODIS bands 2 and 5 to unmix the  
 232 surface reflectance to derive SCF and  $R_{\text{eff}}$  (Figure 2), similar to the approach in Painter  
 233 et al. (2009). The surface reflectance at band  $i$  ( $R_{\text{band } i}^{\text{MODIS}}$ ) can be expressed as follows

234 (Cui et al., 2021, 2023):

$$235 R_{\text{band } i}^{\text{MODIS}} = \frac{E_{\text{band } i} \times \text{SCF} \times R_{\text{band } i}^{\text{MODIS, snow}} + E_{\text{band } i} \times (1 - \text{SCF}) \times R_{\text{band } i}^{\text{soil}}}{E_{\text{band } i}} \\ 236 = \text{SCF} \times R_{\text{band } i}^{\text{MODIS, snow}} + (1 - \text{SCF}) \times R_{\text{band } i}^{\text{soil}}, \quad (2)$$

237 where  $R_{\text{band } i}^{\text{MODIS, snow}}$  and  $R_{\text{band } i}^{\text{soil}}$  represent the snow and soil reflectances at band  $i$ ,  
 238 respectively, with  $R_{\text{band } i}^{\text{soil}}$  taken from Siegmund and Menz (2005), and  $E_{\text{band } i}$  is the  
 239 solar irradiance at band  $i$ . The snow reflectance at band  $i$  ( $R_{\text{band } i}^{\text{MODIS, snow}}$ ) can be  
 240 expressed as

$$241 R_{\text{band } i}^{\text{MODIS, snow}} = \left( \frac{R_{\text{band } i}^{\text{MODIS}} - (1 - \text{SCF}) \times R_{\text{band } i}^{\text{soil}}}{\text{SCF}} \right). \quad (3)$$

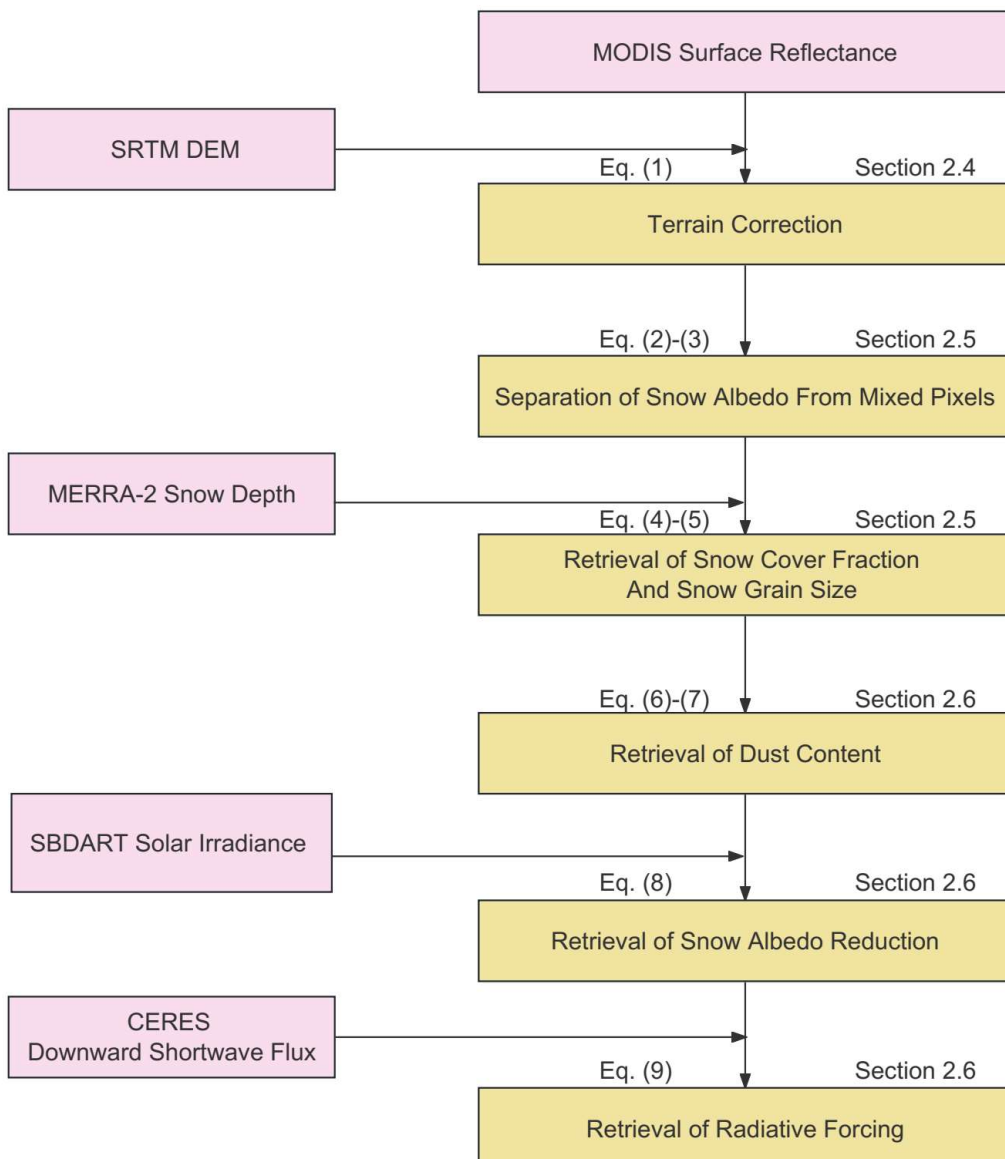
242 We then fit the SNICAR-simulated snow reflectance to the MODIS-derived snow  
 243 reflectance, which is expressed as either

$$244 \text{RMSE} = \left( \frac{1}{2} (a \times (R_{\text{band } 2}^{\text{SNICAR, snow}} - R_{\text{band } 2}^{\text{MODIS, snow}})^2 + (R_{\text{band } 5}^{\text{SNICAR, snow}} - R_{\text{band } 5}^{\text{MODIS, snow}})^2) \right)^{\frac{1}{2}} \quad (4)$$

245 or

$$246 \text{RMSE} = \frac{1}{2} (a \times (R_{\text{band } 2}^{\text{SNICAR, snow}} - \left( \frac{R_{\text{band } 2}^{\text{MODIS}} - (1 - \text{SCF}) \times R_{\text{band } 2}^{\text{soil}}}{\text{SCF}} \right))^2 \\ 247 + (R_{\text{band } 5}^{\text{SNICAR, snow}} - \left( \frac{R_{\text{band } 5}^{\text{MODIS}} - (1 - \text{SCF}) \times R_{\text{band } 5}^{\text{soil}}}{\text{SCF}} \right))^2)^{\frac{1}{2}}, \quad (5)$$

248 where RMSE is the root mean square error,  $R_{\text{band } i}^{\text{SNICAR, snow}}$  is the SNICAR-simulated  
 249 snow reflectance at band  $i$  (which is dependent on the  $R_{\text{eff}}$  and solar zenith angle, where  
 250 the solar zenith angle is derived from the MODIS data), and  $a$  is an empirical coefficient  
 251 (0.1–1 range). In this study,  $a$  was set to 0.1 to reduce the interference of dust on the  
 252 snow properties retrieval because a high dust content can influence the snow albedo at  
 253 band 2 (Figure 1). We can then derive SCF and  $R_{\text{eff}}$  by minimizing the RMSE (Painter  
 254 et al., 2009).



255

256 **Figure 2. Flowchart illustrating the step-by-step retrieval of dust content and the**  
 257 **associated snow albedo reduction and radiative forcing: the pink boxes denote the**  
 258 **external input data, while the yellow boxes are used for calculations in this study.**

259 **2.6 Dust content and snow albedo reduction retrieval**

260 We fit the SNICAR-simulated snow reflectance to the MODIS-derived snow  
 261 reflectance in bands 3 and 4, which are the most sensitive to the dust content in snow,  
 262 following Pu et al. (2019) and Cui et al. (2021), which are expressed as either

263 
$$\text{RMSE} = \frac{1}{2} \left( (R_{\text{band 3}}^{\text{SNICAR, snow}} - R_{\text{band 3}}^{\text{MODIS, snow}})^2 + (R_{\text{band 4}}^{\text{SNICAR, snow}} - R_{\text{band 4}}^{\text{MODIS, snow}})^2 \right)^{\frac{1}{2}} \quad (6)$$

264 or

$$265 \text{ RMSE} = \left( \frac{1}{2} \left( (R_{\text{band 3}}^{\text{SNICAR, snow}} - \left( \frac{R_{\text{band 3}}^{\text{MODIS}} - (1 - \text{SCF}) \times R_{\text{band 3}}^{\text{soil}}}{\text{SCF}} \right))^2 \right)^{\frac{1}{2}} \right. \\ 266 \left. + (R_{\text{band 4}}^{\text{SNICAR, snow}} - \left( \frac{R_{\text{band 4}}^{\text{MODIS}} - (1 - \text{SCF}) \times R_{\text{band 4}}^{\text{soil}}}{\text{SCF}} \right))^2 \right)^{\frac{1}{2}}, \quad (7)$$

267 where  $R_{\text{band 3}}^{\text{SNICAR, snow}}$  is a function of four factors: dust content,  $R_{\text{eff}}$ , snow depth, and  
268 solar zenith angle. The latter three factors have been derived, leaving the dust content  
269 as the only unknown. Therefore, the dust content can be retrieved by minimizing Eq.  
270 (7). We assume that the derived dust content in this study accounts for the total light  
271 absorption by all of the LAPs that are present in the snowpack. This is because our  
272 study area is close to the Taklamakan Desert (TD), where large amounts of dust  
273 accumulate on the snow surface annually. In contrast, anthropogenic activities and  
274 biomass burning are rare, resulting in limited depositions of black carbon (BC) and  
275 organic carbon (OC) (Fig. S8). Observations from snow and atmosphere have  
276 confirmed this phenomenon (Wake et al., 1994; Huang et al., 2007). Therefore, our  
277 assumption is plausible.

278 The dust-induced broadband albedo reduction ( $\Delta\alpha$ ) can then be calculated as follows:

$$279 \Delta\alpha = \frac{\sum_{\lambda=300\text{nm}}^{\lambda=2500\text{nm}} E_{\lambda} \cdot (R_{\lambda}^{\text{SNICAR, pure-snow}} - R_{\lambda}^{\text{SNICAR, snow}}) \cdot \Delta\lambda}{\sum_{\lambda=300\text{nm}}^{\lambda=2500\text{nm}} E_{\lambda} \cdot \Delta\lambda}, \quad (8)$$

280 Where  $R_{\lambda}^{\text{SNICAR, pure-snow}}$  and  $R_{\lambda}^{\text{SNICAR, snow}}$  are the SNICAR-simulated pure and  
281 polluted snow albedo using snow grain size and dust content retrieved above, solar  
282 zenith angle from MODIS and snow depth from MERRA2, respectively.  $E_{\lambda}$  represents  
283 the spectral solar irradiance at wavelength  $\lambda$  simulated from the SBDART model,  $\Delta\lambda$  is  
284 10 nm, and  $R_{\lambda}^{\text{SNICAR, pure-snow}}$  and  $R_{\lambda}^{\text{SNICAR, snow}}$  are the SNICAR-simulated pure and  
285 polluted snow albedo, respectively. The spectral irradiance from SBDART is only used  
286 for integrating the spectral MODIS albedo to achieve broadband albedo. Thus, the  
287 uncertainty in solar irradiance from the assumed atmospheric properties has limited  
288 influence on the retrieval of snow albedo reduction (Cui et al., 2021).

289 The dust-induced radiative forcing (RF) is calculated as follows:

290  $RF = \Delta\alpha \cdot SW$ , (9)

291 where SW is the downward shortwave flux, which is obtained from CERES.

292 The in situ dust content was not measured to verify the MODIS retrievals because of  
293 the challenging geographical conditions surrounding the TD. Nevertheless, Cui et al.  
294 (2021) verified a similar retrieval method across the Northern Hemisphere. They  
295 considered that the accuracy of MODIS surface reflectance is typically  $\pm (0.005 + 0.05$   
296  $\times$  reflectance) under conditions where aerosol optical depth (AOD) is less than 5.0, and  
297 solar zenith angle is less than  $75^\circ$ , as stated in the MODIS Surface Reflectance user's  
298 guide (Collection 6; <https://modis.gsfc.nasa.gov/data/dataproducts/mod09.php>, last access:  
299 19 January, 2024). In addition, the bias for snow grain size retrieval was assumed to be  
300 30 % according to the studies of Pu et al. (2019) and Wang et al. (2017). These biases  
301 led to an overall uncertainty ranging from 10% to 110% in the retrieval of LAPs across  
302 the Northern Hemisphere. The study revealed that uncertainty decreased as LAPs  
303 concentration increased, with reported uncertainties dropping to below approximately  
304 30% in regions of high pollution, such as Northeast China. In our study, the snowpack  
305 was also significantly polluted due to severe dust depositions, leading us to consider a  
306 retrieval uncertainty of 30% for LAPs, in alignment with the findings of Cui et al.  
307 (2021). Then, the overall lower bound and upper bound of the uncertainty value of snow  
308 albedo reduction retrieval was calculated and will be discussed in the following section.  
309 Moreover, we utilized the LAPs and the corresponding albedo reduction retrieved at  
310 the local time of 10:30 AM (the time of the MODIS Terra satellite overpass), as the  
311 proxy for daily averages following Painter et al. (2012). This approximation was  
312 reasonable, given that the content of LAPs exhibited little variation over a diurnal cycle  
313 (Painter et al., 2009; Zege et al., 2011). The variation in snow albedo throughout the  
314 day was primarily attributed to changes in the solar zenith angle (Figure S1). Since the  
315 solar zenith angle predominantly influences snow albedo in NIR, with little impact on  
316 the VIS, the diurnal variation in LAPs-induced snow albedo reduction was also  
317 considered limited.

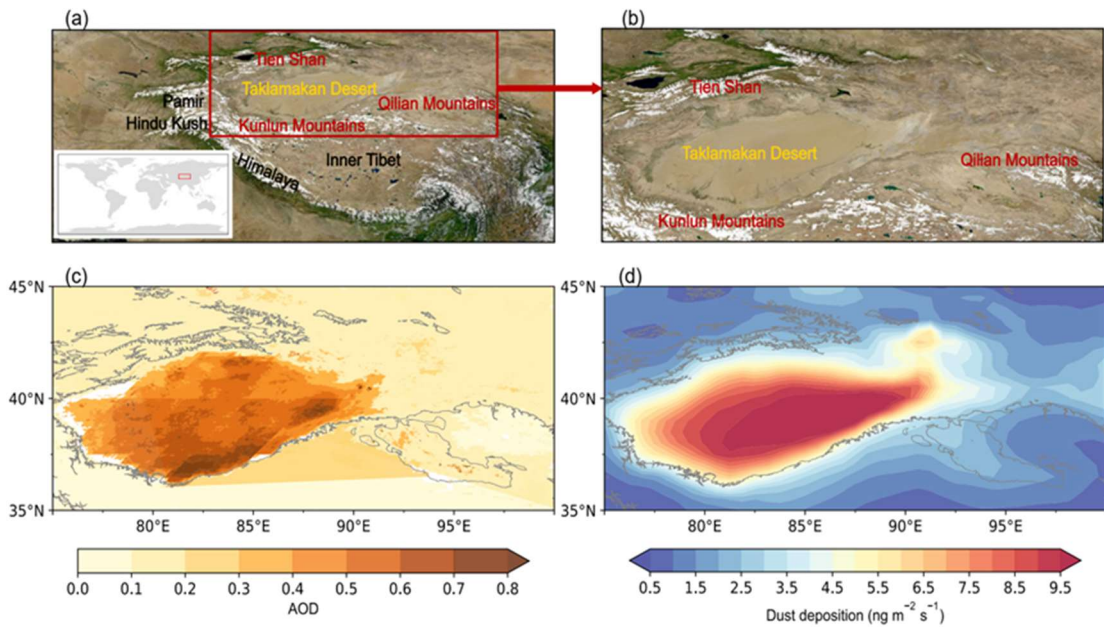
318 As noted above, the snow albedo reduction is mainly dependent on the dust content,  
319  $R_{eff}$ , snow depth, and solar zenith angle. The  $R_{eff}$  and snow depth can be categorized as

320 snow properties. We compared the dust content, snow properties, and solar zenith angle  
321 to discuss their contributions to the spatial variations in snow albedo reduction (Pu et  
322 al., 2019; Cui et al., 2021). The supplementary information contains a thorough  
323 derivation of this method.

324 **3 Results**

325 **3.1 Remote sensing of the snow darkening effect across the high mountains  
326 surrounding the TD**

327 The TD is located in the northern part of HMA and is surrounded by some of the highest  
328 mountain ranges on Earth, including the Kunlun Mountains, Tien Shan, and Pamir  
329 (Figures 3a and b). The TD region emits vast amounts of dust particles into the  
330 atmosphere each year, particularly during the spring and summer (Wang et al., 2008;  
331 Chen et al., 2013, 2017b; Kang et al., 2016; Wu et al., 2021; Tang et al., 2022); this  
332 phenomenon is confirmed by the high AOD levels at 550 nm from March to August  
333 (Figure 3c). A significant amount of this dust is ultimately redeposited across the Tarim  
334 Basin and the surrounding mountains. The Tien Shan and Kunlun Mountains are two  
335 regions that experience high levels of dust deposition owing to the local topography  
336 and atmospheric circulation patterns (Figure 3d) (Huang et al., 2007, 2014; Ge et al.,  
337 2014; Dong et al., 2022). Therefore, we selected two typical cases to demonstrate the  
338 snow-darkening effect across the mountains surrounding the TD, a springtime dust  
339 event across the Tien Shan and a summertime dust event across the Kunlun Mountains.



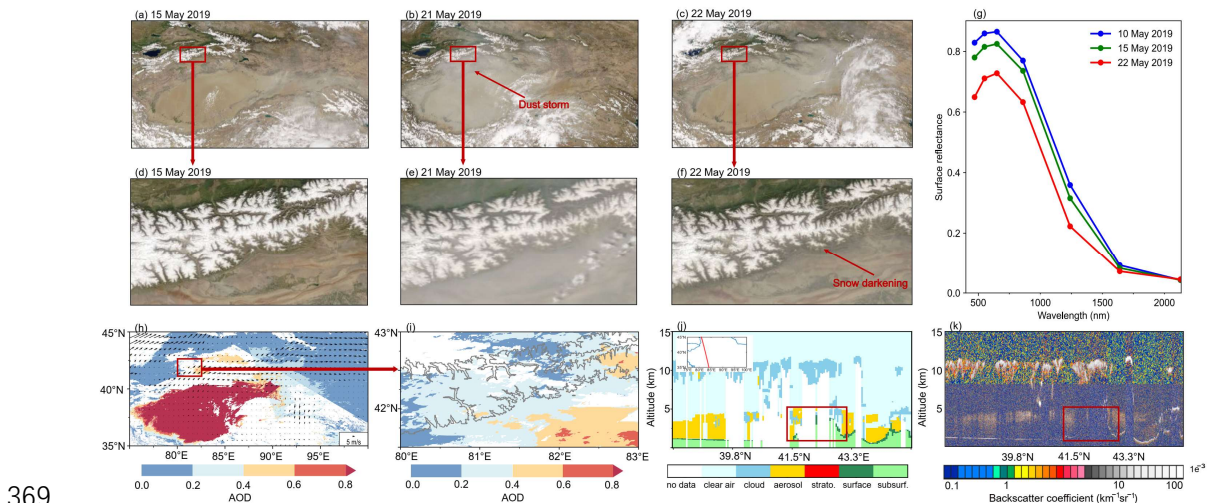
340

341 **Figure 3. Mountain ranges surrounding the Taklamakan Desert, and AOD and**  
 342 **dust deposition distributions across the Taklamakan Desert and surrounding**  
 343 **region. (a, b) Geographic location of the Taklamakan Desert and surrounding**  
 344 **mountains. The red box defines the area in (b). Spatial distributions of the**  
 345 **averaged (c) AOD and (d) dust deposition values, which were derived from**  
 346 **MCD19A2 and MERRA-2 during the March to August 2019 period.**

347 **3.1.1 Dust-induced snow darkening across the Tien Shan**

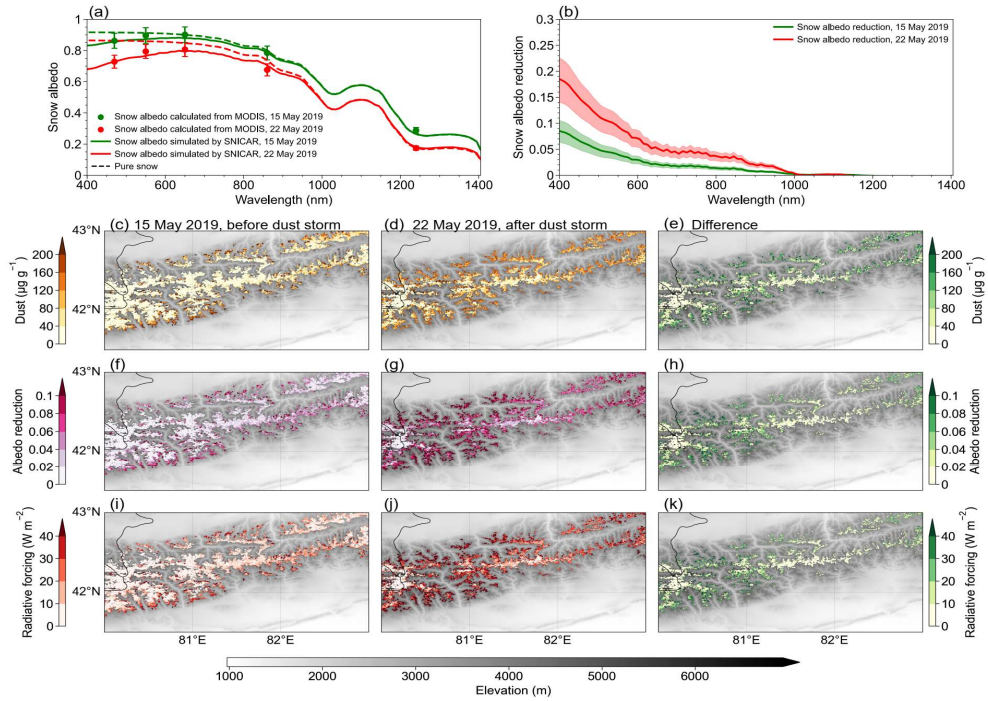
348 A significant dust storm occurred across the TD region on 18–22 May 2019 (Figures 4  
 349 and S2). The 21 May 2019 Terra/MODIS satellite image (Figure 4b) showed that the  
 350 dust plumes had spread to the north and east owing to an upper anticyclone system in  
 351 the Tarim Basin (Figure 4h). Some dust particles were uplifted to >4 km altitude, as  
 352 shown in the CALIPSO aerosol vertical profiles (Figures 4j and k). These dust particles  
 353 were then transported to the snow-covered high-elevation areas of the Tien Shan, as  
 354 illustrated in the MODIS AOD images (Figures 4h and i). Dust plumes were also  
 355 observed in a satellite image that spanned the broadly snow-covered central Tien Shan  
 356 (Figure 4e), and the snow appeared to darken in the 22 May 2019 Terra/MODIS satellite  
 357 image that was acquired under the first clear-sky conditions after this severe dust event.  
 358 However, the snow was much whiter prior to the passage of this dust storm, as shown  
 359 in Figures 4d and f. Figure 4g further illustrates changes in the surface reflectance of

360 the snow-covered areas, providing a more intuitive influence of dust deposition on the  
 361 snow physical properties. The reflectance was around 0.8 in the VIS spectrum on 15  
 362 May 2019, but quickly decreased to  $<0.7$  on 22 May 2019, after the passage of the dust  
 363 plumes. The reduction in VIS wavelengths was up to  $>0.1$  during this short time interval.  
 364 These observations show that the dust plumes from the TD can significantly darken the  
 365 snowpack across the Tien Shan through heavy dust deposition. Furthermore, the  
 366 progression of air-temperature-induced snow aging cannot effectively explain this  
 367 phenomenon. This result is consistent with previous satellite observations over the  
 368 Himalayas (Gautam et al., 2013).



370 **Figure 4. Satellite observations during the 18–22 May 2019 severe dust event**  
 371 **across the Tien Shan. (a, d) Terra/MODIS satellite true-color images acquired on**  
 372 **15 May 2019, prior to the dust storm. (b, e) Terra/MODIS satellite images**  
 373 **acquired on 21 May 2019, with the dust storm transport from the TD to the Tien**  
 374 **Shan indicated by the red arrow in (b). (c, f) Terra/MODIS satellite images**  
 375 **acquired on 22 May 2019, with significant snow darkening observed across the**  
 376 **Tien Shan after the dust storm. (g) MOD09GA spectral surface reflectance across**  
 377 **snow-covered areas on 10 May 2019 (blue), 15 May 2019 (green), and 22 May 2019**  
 378 **(red). (h) MODIS AOD image on 21 May 2019, with the ERA5 daily mean wind**  
 379 **vector at 700 hPa overlain. (i) MODIS AOD image across the Tien Shan on 21**  
 380 **May 2019. Gray lines denote the 3000 m elevation contour. CALIPSO (j) vertical**  
 381 **feature mask and (k) backscatter coefficient on 21 May 2019.**

382 We also derived the spectral snow albedo and retrieved several parameters to  
383 quantitatively assess the impact of this dust deposition on snow darkening. The  
384 SNICAR-simulated spectral snow albedo (solid lines) and MODIS-derived 5-band  
385 snow albedo (dots) in Figure 5a are averaged over the area in Figure 5c. These results  
386 demonstrate an agreement of >95%, thereby indicating the reliability of our retrievals.  
387 The spectral snow albedo reduction on 15 and 22 May 2019 are shown in Figure 5b.  
388 There were significant increases in the albedo reductions as the wavelength decreased,  
389 particularly on 22 May 2019, which is consistent with theoretical simulations of the  
390 dust-induced snow darkening effect (Figure 1). However, the spectral curve differed  
391 from the BC-induced results in the anthropogenically influenced areas of Northeast  
392 China (Wang et al., 2017; Niu et al., 2022) and Northwest China (Shi et al., 2020).  
393 Therefore, we indicate that the observed snow darkening in this study was mainly  
394 caused by natural dust emissions, as opposed to BC and organic carbon (OC) emissions  
395 from anthropogenic activities and/or biomass burning. There was a spectral snow  
396 albedo reduction of 0.02–0.08 in the VIS on 15 May 2019, which represents persistent  
397 but relatively low dust deposition during spring. However, the severe dust event caused  
398 a rapid increase in spectral snow albedo reduction to 0.045–0.18 in a matter of days.  
399 The approximate doubling of the albedo reduction indicates that the increase in the dust  
400 concentration was much greater than 100% based on the nonlinear theory of the snow  
401 albedo feedback to the dust concentration (Figure 1). This implies that it is important  
402 to consider both the frequency and intensity of dust events when examining their impact  
403 on snow albedo. Similar phenomena that were induced by catastrophic wildfire events  
404 have been observed in the snowpack across New Zealand (Pu et al., 2021). These results  
405 suggest that extreme events may reflect the more pronounced impact of climate  
406 warming on our planet (Liang et al., 2021; Gui et al., 2022). Therefore, it is important  
407 to pay more attention to extreme events, rather than just conducting either annual or  
408 monthly averaged analyses, to fully capture the influence of climate change on snow  
409 albedo.



410

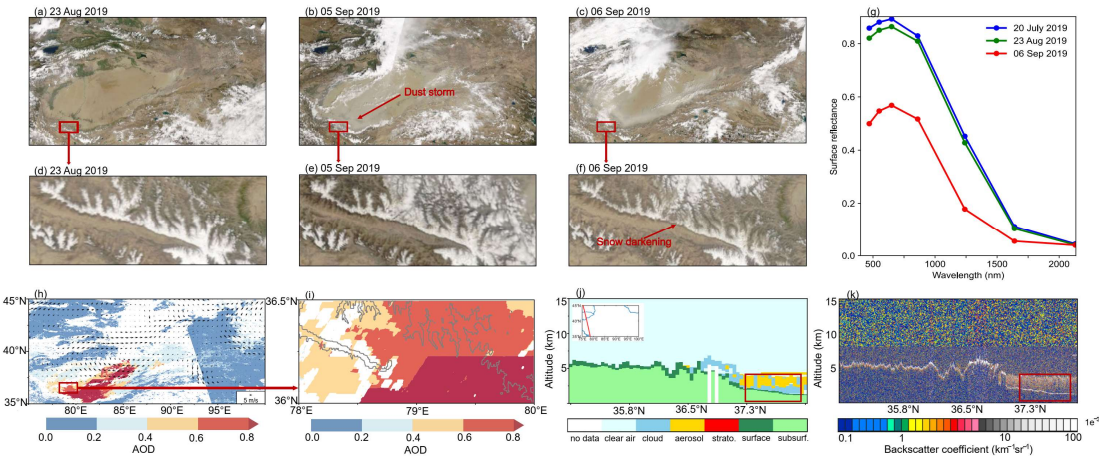
411 **Figure 5. (a)** Averaged SNICAR-simulated spectral snow albedo (solid lines) and  
 412 MODIS-derived 5-band snow albedo (dots) for the region across the Tien Shan  
 413 impacted by the 18–22 May 2019 severe dust event. **(b)** Snow albedo reduction on  
 414 15 May 2019 (green) and 22 May 2019 (red). Shadows indicate the retrieval  
 415 uncertainty. Spatial distributions of the average **(c, d)** dust, **(f, g)** albedo reduction,  
 416 and **(i, j)** radiative forcing on 15 and 22 May 2019, respectively. Spatial  
 417 distributions of the differences in **(e)** dust, **(h)** albedo reduction, and **(k)** radiative  
 418 forcing between 15 and 22 May 2019. The background image in **(c–k)** is a grayscale  
 419 topographic map of the Tien Shan.

420 Figures 5c and d illustrate the spatial distributions of the dust concentration in the  
 421 snowpack on 15 and 22 May 2019, respectively. There was a sharp increase in the dust  
 422 content from 2–55 to 42–192  $\mu\text{g g}^{-1}$  ( $\sim 2.67$ -fold increase) following the severe dust  
 423 event, with the lower elevations possessing higher dust concentrations and greater dust  
 424 content increases (Figures 5d, 5e and S3). Snow darkening was observed across all of  
 425 the snow-covered areas ( $> 2100 \text{ km}^2$ ), including the summits, thereby highlighting the  
 426 extensive influence of this severe dust event across the central Tien Shan. Furthermore,  
 427 these results demonstrate the capability and effectiveness of employing satellite remote  
 428 sensing to observe/monitor large-scale snow darkening. The dust-induced broadband

429 snow albedo reductions and radiative forcing are shown in Figures 5f–k, with observed  
430 spatial patterns that are largely similar to the dust content distributions. The snow  
431 albedo reduction increased by 0.008–0.052, with an observed increase from 0.002–  
432 0.032 on 15 May to 0.028–0.079 on 22 May. The radiative forcing increased by 2.5–  
433 20.5 W m<sup>-2</sup>, with an observed increase from 0.5–12.5 W m<sup>-2</sup> on 15 May to 11–31.5 W  
434 m<sup>-2</sup> on 22 May (Figure S4). Both the snow albedo reduction and radiative forcing  
435 increased by a factor of ~2.39, which directly reflects its significant impact on the  
436 regional radiation balance and climate (Dumont et al., 2020). Snow darkening can also  
437 accelerate snow aging by absorbing more shortwave radiation in a warming spring, as  
438 characterized by the  $R_{\text{eff}}$  growth (Figures S3a–c). Figure S5a-d show the overall  
439 uncertainty in snow albedo reduction retrieval in Tien Shan, with the uncertainty  
440 bounds averaging 24% (-26%) on 15 May and 22% (-24%) on 22 May, respectively.  
441 As the dust content increases, the uncertainty in the snow albedo reduction decreases.

#### 442 **3.1.2 Dust-induced snow darkening across the Kunlun Mountains**

443 The Kunlun Mountains are located along the southern (northern) edge of the Tarim  
444 Basin (Tibetan Plateau). The northern slope of the Central/West Kunlun Mountains  
445 directly faces the TD (Figure 1a) and should have experienced the most severe dust-  
446 induced snow darkening. Similar conditions also exist across the Himalayas, where the  
447 south slope faces both the Thar Desert in India and the Middle East. We captured a  
448 typical dust storm event with associated dust deposition and snow darkening that  
449 occurred between 5 and 11 May 2020 along the northern slope of the Kunlun Mountains  
450 using MODIS satellite images (Figure S6). The previously mentioned spring  
451 phenomenon is well-known due to intense springtime dust emissions from the TD,  
452 whereas the summer phenomenon is usually overlooked. However, it has been shown  
453 that dust can more effectively cross the Kunlun Mountains during the summer months,  
454 with the potential to induce changes in atmospheric dynamics and thermal effects (Yuan  
455 et al., 2018). Therefore, we specifically chose a summer case to highlight snow  
456 darkening across the Kunlun Mountains.

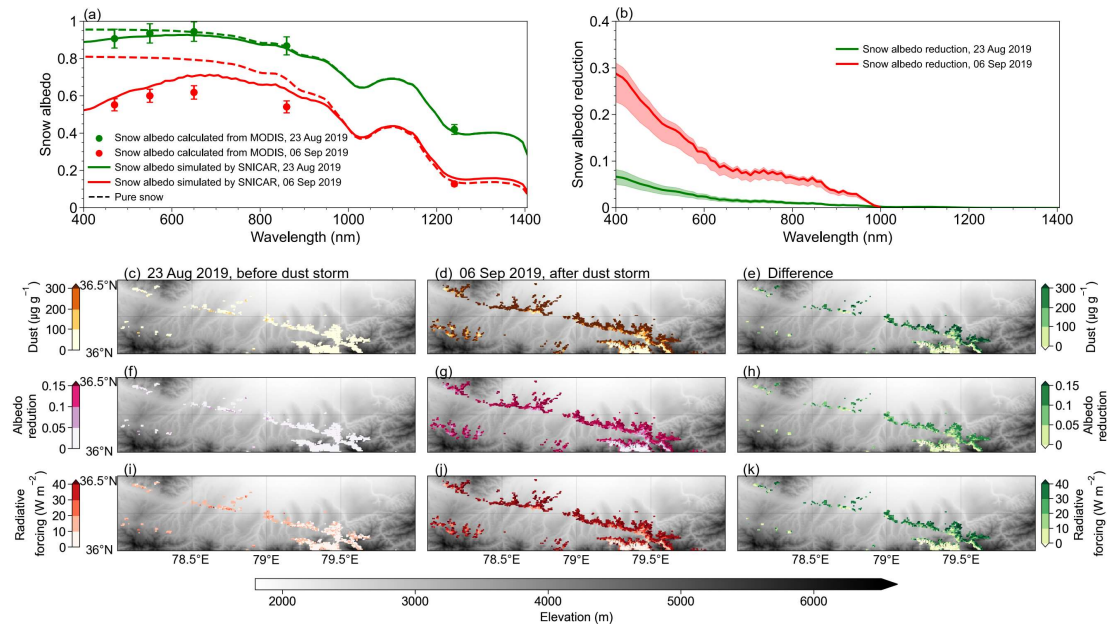


457

458 **Figure 6. Satellite observations during the 26 Aug to 08 Sep 2019 dust storm across**  
459 **the Kunlun Mountains. (a, d) Terra/MODIS satellite true-color images acquired**  
460 **on 23 Aug 2019, prior to the dust storm. (b, e) Terra/MODIS satellite images**  
461 **acquired on 05 Sep 2019, with the dust storm transport from the TD to the Kunlun**  
462 **Mountains indicated by the red arrow in (b). (c, f) Terra/MODIS satellite images**  
463 **acquired on 06 Sep 2019, with significant snow darkening across the Kunlun**  
464 **Mountains after the dust storm. (g) MOD09GA spectral surface reflectance over**  
465 **the snow-covered areas on 20 July 2019 (blue), 23 Aug 2019 (green), and 06 Sep**  
466 **2019 (red). (h) MODIS AOD image on 05 Sep 2019, with the ERA5 daily mean**  
467 **wind vector at 700 hPa overlain. (i) MODIS AOD image across the Kunlun**  
468 **Mountains on 05 Sep 2019. Gray lines denote the 3000-m elevation contour.**  
469 **CALIPSO (j) vertical feature mask and (k) backscatter coefficient on 04 Sep 2019.**

470 A significant dust event that impacted the northern slope of the Kunlun Mountains  
471 occurred from 26 Aug to 08 Sep 2019 (Figures 6b and S7). The Terra/MODIS satellite  
472 images on 5 Sep 2019 (Figures 6b and e) show the accumulation of dust plumes along  
473 the southern edge of the Tarim Basin. In summer, the westerlies weaken and shift to  
474 the north, leading to more accumulation of dust locally instead of transporting it  
475 eastward (Chen et al., 2017a; Yuan et al., 2018). Furthermore, the enhanced sensible  
476 heat flux favors the southward transport of uplifted dust, leading to cyclonic  
477 convergence at the surface and anticyclonic divergence at the top of the troposphere  
478 above the TD (Figure 6h). The synergistic effects of atmospheric dynamic and thermal

479 forcing can cause the dust plumes to be uplifted to  $\sim$ 5 km altitude (Figures 6j–k). This  
 480 uplift effectively facilitated the dust plume ascent to the snow-covered areas across the  
 481 northern slope of the Kunlun Mountains (Figure 6e and i). A comparison of the MODIS  
 482 images that were acquired on 23 Aug and 6 Sep 2019 highlighted snow darkening after  
 483 this severe dust storm (Figures 6d and f). The surface reflectance decreased by  $\sim$ 0.22  
 484 in the VIS spectrum, decreasing from 0.285 on 23 Aug to  $\sim$ 0.065 on 5 Sep. These  
 485 observations indicate that this summertime dust event caused significant snow  
 486 darkening across the Kunlun Mountains.



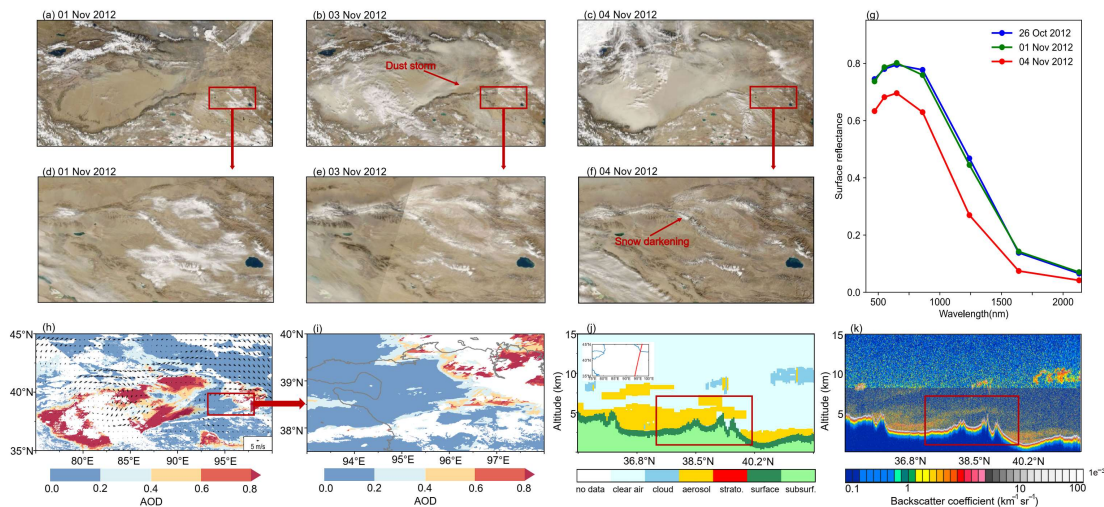
487  
 488 **Figure 7. (a)** Averaged SNICAR-simulated spectral snow albedo (solid lines) and  
 489 MODIS-derived 5-band snow albedo (dots) for the region across the Kunlun  
 490 Mountains impacted by the 26 Aug to 08 Sep 2019 severe dust event. **(b)** Snow  
 491 albedo reductions on 23 Aug 2019 (green) and 06 Sep 2019 (red). Shadows indicate  
 492 the retrieval uncertainty. Spatial distributions of the average **(c, d)** dust, **(f, g)**  
 493 albedo reduction, and **(e, j)** radiative forcing on 23 Aug and 06 Sep 2019,  
 494 respectively. Spatial distributions of the differences in **(e)** dust, **(h)** albedo reduction,  
 495 and **(k)** radiative forcing between 23 Aug and 06 Sep 2019. The background image  
 496 in **(c–k)** is a grayscale topographic map of the Kunlun Mountains.

497 Figure 7 provides a more quantitative investigation of the impact of this severe dust  
 498 event on the snowpack across the Kunlun Mountains, whereby a significant increase in

499 dust content from 12–50  $\mu\text{g g}^{-1}$  on 23 Aug to 170–360  $\mu\text{g g}^{-1}$  on 06 Sep (~6.45-fold  
500 increase) is observed after this severe dust event (Figure S8). The darkened snow-  
501 covered area spans  $>600 \text{ km}^2$ , with a clear south–north gradient in the dust  
502 concentration distribution that is influenced by both the orientation and elevation of the  
503 mountains. This large dust deposition induced a 0.015–0.106 increase in snow albedo  
504 reduction, with an observed increase from 0.013–0.032 on 23 Aug to 0.088–0.136 on  
505 06 Sep. There was also a substantial increase in radiative forcing of  $4.1\text{--}37.5 \text{ W m}^{-2}$ ,  
506 with an observed increase from  $3\text{--}11 \text{ W m}^{-2}$  on 23 Aug to  $31\text{--}49 \text{ W m}^{-2}$  on 06 Sep  
507 (Figure S4). Note that these increases in both the snow albedo reduction and radiative  
508 forcing are approximately two times larger than those observed over the Tien Shan  
509 (Figure S3 and S8). These findings indicate accelerated snow aging, as evidenced by  
510 the faster growth rate of the  $R_{\text{eff}}$  observed across the Kunlun Mountains (Figures S9).  
511 Furthermore, Figure S5e-h show the overall uncertainty in snow albedo reduction  
512 retrieval in Kunlun Mountains, with the uncertainty bounds averaging 23% (-25%) on  
513 23 Aug and 7% (-21%) on 06 Sep, respectively. Notably, compared to the Tien Shan  
514 dust event described in Section 3.1.1, the Kunlun Mountains event demonstrates a more  
515 significant reduction in the uncertainty of snow albedo reduction as the dust content  
516 increases, especially in the upper bound of the uncertainty. This observation aligns with  
517 findings reported by Cui et al. (2021).

### 518 **3.1.3 Snow darkening across the Qilian Mountains**

519 Unlike the Tien Shan and Kunlun Mountains, the Qilian Mountains are located  
520 approximately 1000 km east of the Tarim Basin. The Hexi Corridor, a narrow and  
521 relatively flat plain that lies between the high-elevation, inhospitable terrains of the  
522 Mongolian and Tibetan plateaus (see Figure 3), is situated to the north of the Qilian  
523 Mountains. The unique terrain of the region results in TD dust plumes following a  
524 preferred transport route across the Hexi Corridor to East Asia (Zhang et al., 2008;  
525 Meng et al., 2018). These dust plumes are generally uplifted to  $>4 \text{ km}$  altitude and  
526 entrained in the westerlies (Huang et al., 2008; Dong et al., 2014; Chen et al., 2022),  
527 thereby providing a means for dust deposition onto the snowpack across the Qilian  
528 Mountains.



531 **Figure 8. Satellite observations during the 02–04 Nov 2012 dust storm across the**  
 532 **Qilian Mountains. (a, d) Terra/MODIS satellite true-color images acquired on 01**  
 533 **Nov 2012, prior to the dust storm. (b, e) Terra/MODIS satellite images acquired**  
 534 **on 03 Nov 2012, with the dust transport from the TD to the Qilian Mountains**  
 535 **indicated by the red arrow in (b). (c, f) Terra/MODIS satellite images acquired on**  
 536 **04 Nov 2012, with significant snow darkening observed across the Qilian**  
 537 **Mountains after the dust storm. (g) MOD09GA spectral surface reflectance over**  
 538 **the snow-covered areas on 26 Oct 2012 (blue), 01 Nov 2012 (green), and 04 Nov**  
 539 **2012 (red). (h) MODIS AOD image on 03 Nov 2012, with the ERA5 daily mean**  
 540 **wind vector at 700 hPa overlain. (i) MODIS AOD image across the Qilian**  
 541 **Mountains on 03 Nov 2012. The gray line denotes the 3000-m elevation contour.**  
 542 **CALIPSO (j) vertical feature mask and (k) backscatter coefficient on 03 Nov 2012.**

543 Figure 8 illustrates a severe dust event that occurred from 02 to 04 Nov 2012 (Figure  
 544 S10), when abundant dust plumes were being transported across the narrow Hexi  
 545 Corridor (Figures 8b and h). The dust content was much more intense in this region,  
 546 possessing AOD levels of up to  $>0.8$ . Furthermore, the CALIPSO observations  
 547 indicated that the dust plumes were uplifted to  $\sim 10$  km altitude (Figures 8j and k),  
 548 thereby allowing some dust particles to cross over the northern slopes of the Qilian  
 549 Mountains and spread across its western extent (Figures 8e and i). The average

reflectance in the VIS spectrum was stable at around 0.7–0.8 across the snow-covered areas about a week before the severe dust event but then significantly decreased to 0.6–0.7 owing to heavy dust deposition

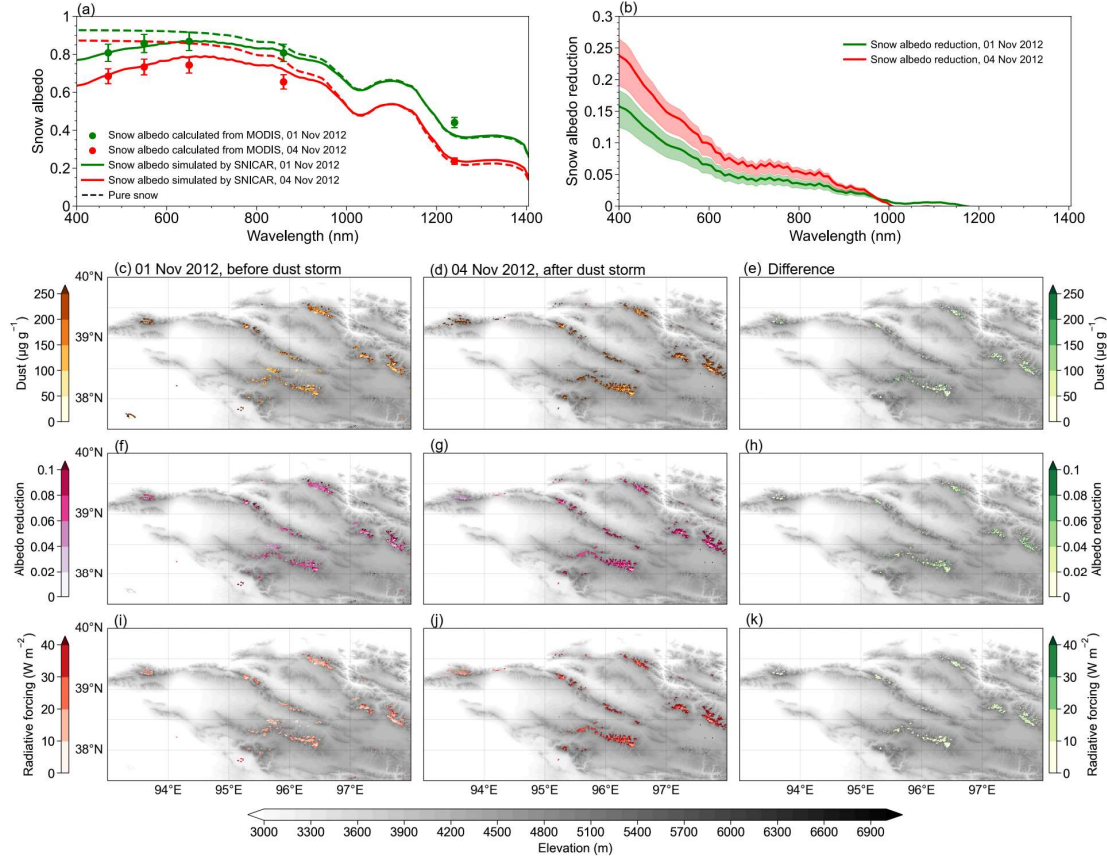


**Figure 9. (a)** Averaged SNICAR-simulated spectral snow albedo (solid lines) and MODIS-derived 5-band snow albedo (dots) for the region across the Qilian Mountains impacted by the 02–04 Nov 2012 severe dust event. **(b)** Snow albedo reductions on 01 Nov 2012 (green) and 04 Nov 2012 (red). Shadows indicate the retrieval uncertainty. Spatial distributions of the average **(c, d)** dust, **(f, g)** albedo reduction, and **(i, j)** radiative forcing on 01 and 04 Nov 2012, respectively. Spatial distributions of the differences in **(e)** dust, **(h)** albedo reduction, and **(k)** radiative forcing between 01 and 04 Nov 2012. The background image in **(c–k)** is a grayscale image of the Qilian Mountains.

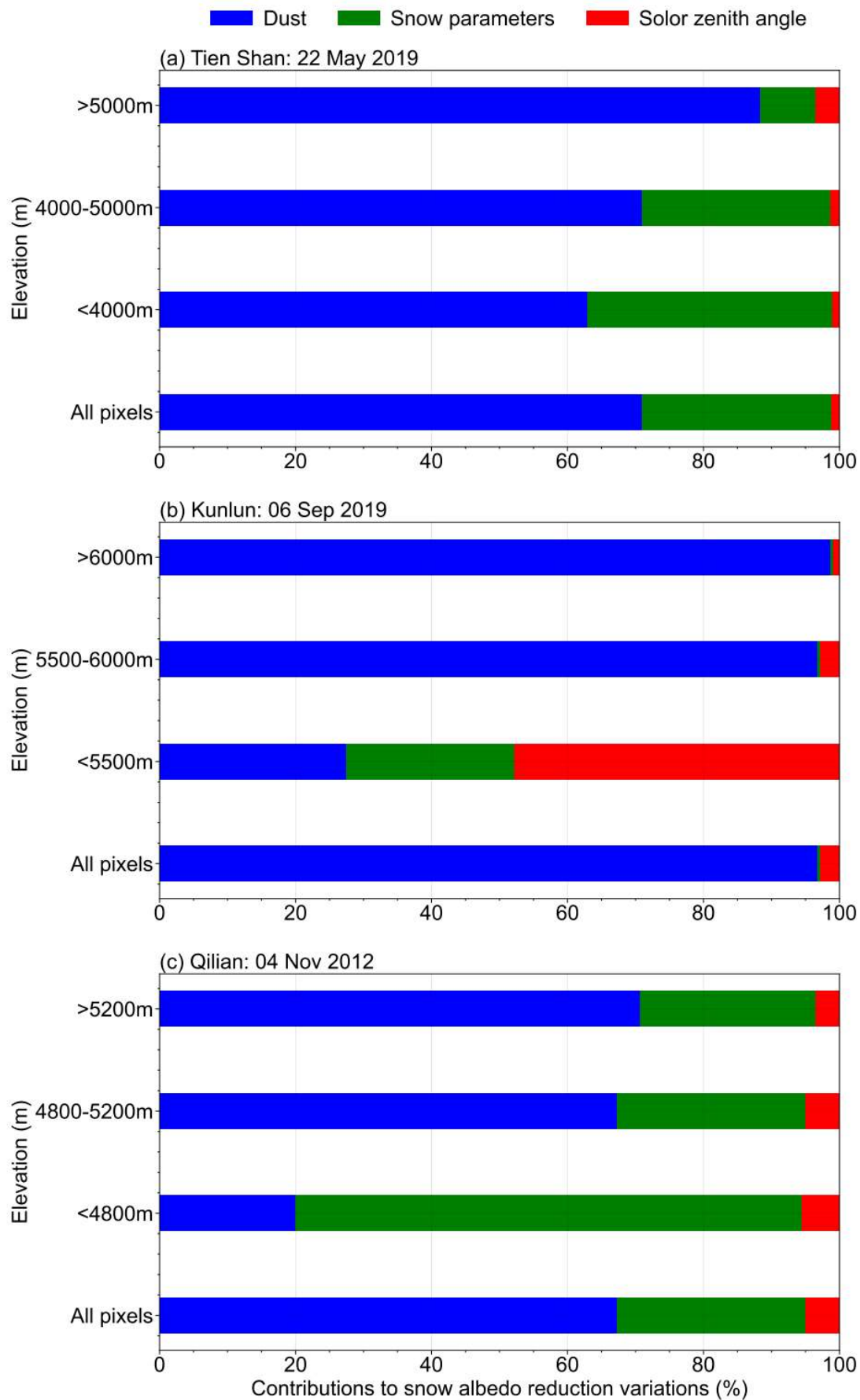
Figure 9 presents the quantitative satellite-derived results, which highlight a rapid increase in dust content from 110–228 to 194–360  $\mu\text{g g}^{-1}$  ( $\sim$ 1.53-fold increase) that spanned a snow-covered area of  $>630 \text{ km}^2$  (Figures 9f–h). This significant increase in

566 dust content led to a considerable increase in snow albedo reduction (radiative forcing)  
567 of  $0.018\text{--}0.067$  ( $3\text{--}16\text{ W m}^{-2}$ ), which increased from  $0.042\text{--}0.076$  ( $11\text{--}20\text{ W m}^{-2}$ ) on 1  
568 Nov 2012 to  $0.092\text{--}0.153$  ( $22\text{--}38\text{ W m}^{-2}$ ) on 4 Nov 2012 (Figure S4). This  $>1.5$ -fold  
569 increase in snow albedo reduction (radiative forcing) was not solely due to the  
570 deposition of dust (Figure S11). Accelerated snow aging, which was observed from the  
571 enhanced  $R_{\text{eff}}$  growth (Figure S9), also contributed to the observed increase in snow  
572 albedo reduction (radiative forcing); this trend was similar to that observed across the  
573 Kunlun Mountains. Figure S5i-1 show the overall uncertainty in snow albedo reduction  
574 retrieval in Qilian Mountains, with the uncertainty bounds averaging 16% (-21%) on  
575 01 Nov and 11% (-20%) on 04 Nov, respectively. Our approach uses satellite remote  
576 sensing to obtain a more complete spatiotemporal evolution of the TD dust storm,  
577 including its emission, long-range transport, and deposition, across the Qilian  
578 Mountains, which offers advantages over previous field measurements (Wei et al.,  
579 2017).

580 **3.2 Contributions to the spatial and altitudinal variations in dust-induced snow  
581 darkening**

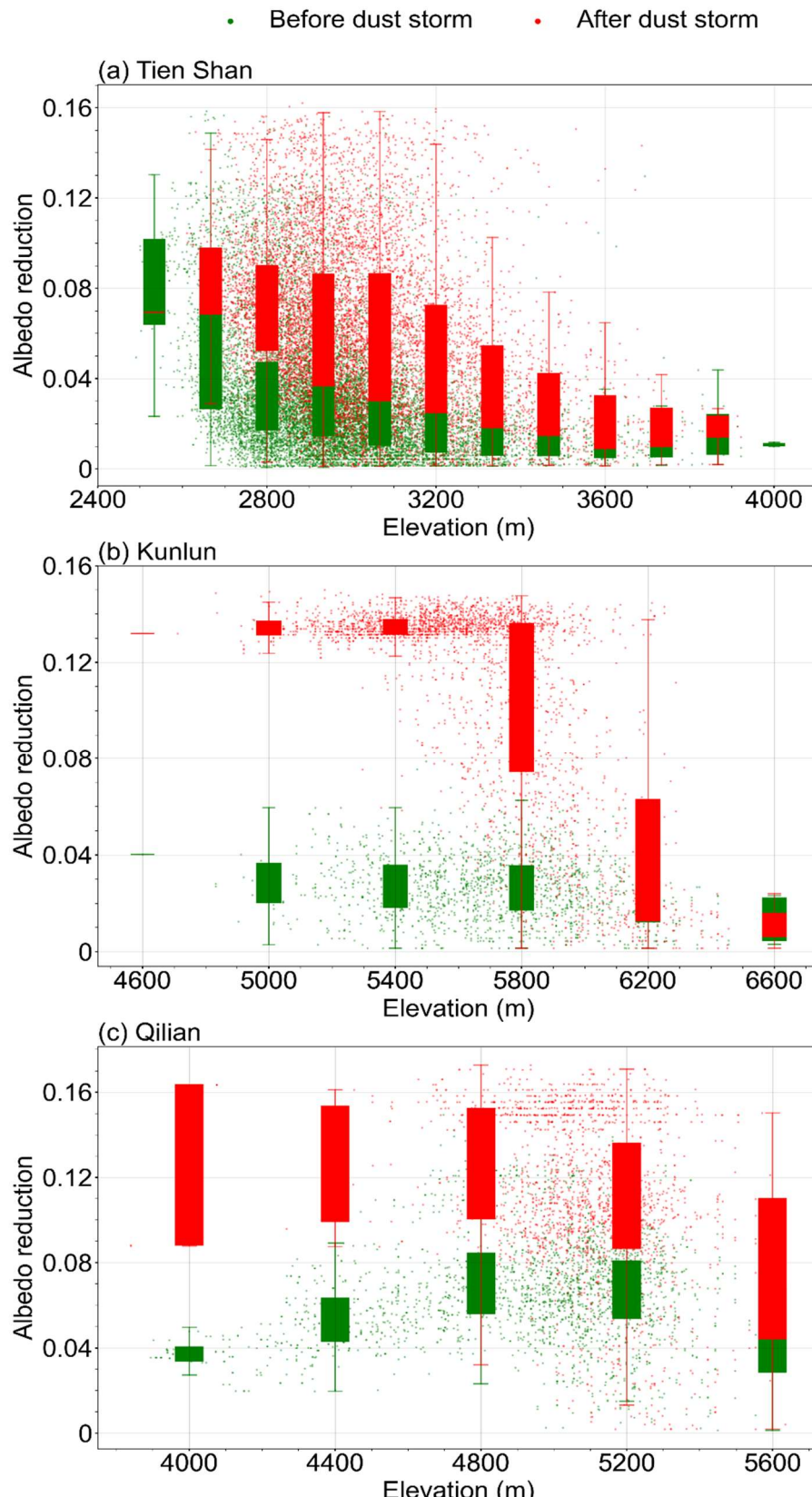
582 We quantified the contributions of the three key factors (dust content, snow properties,  
583 and solar zenith) to the spatial variations in snow albedo reduction (Figure 10) using  
584 the method described in Section 2.6. The dust content was the dominant contributor to  
585 the spatial variations in snow darkening. This is at least partially attributed to the greater  
586 spatial differences in dust content compared with those of the other factors, as shown  
587 in Figures 5, 7, and 9. Furthermore, theoretical modeling has indicated that the snow  
588 albedo reduction is more sensitive to changes in dust content than to changes in the  
589 snow properties and solar zenith angle (Flanner et al., 2021; Usha et al., 2022; Zhao et  
590 al., 2022). Laboratory experiments also support these findings (Zhang et al., 2018; Li  
591 et al., 2022). The contribution of the dust content also increased as the elevation in each  
592 mountain range increased, whereas a decreasing trend was observed for the snow  
593 parameters. This is because the dust content exhibits spatial differences across all of the  
594 elevations owing to its widespread and heterogeneous depositions. However, the snow  
595 depth has a more semi-infinite nature and  $R_{\text{eff}}$  exhibits greater spatial homogeneity at

596 higher elevations owing to slower snow aging.



598 **Figure 10. Contributions of the spatial variations in dust content (blue), snow  
599 parameters (green), and solar zenith angle (red) to the snow albedo reduction at  
600 different elevations across the (a) Tien Shan, (b) Kunlun Mountains, and (c) Qilian  
601 Mountains.**

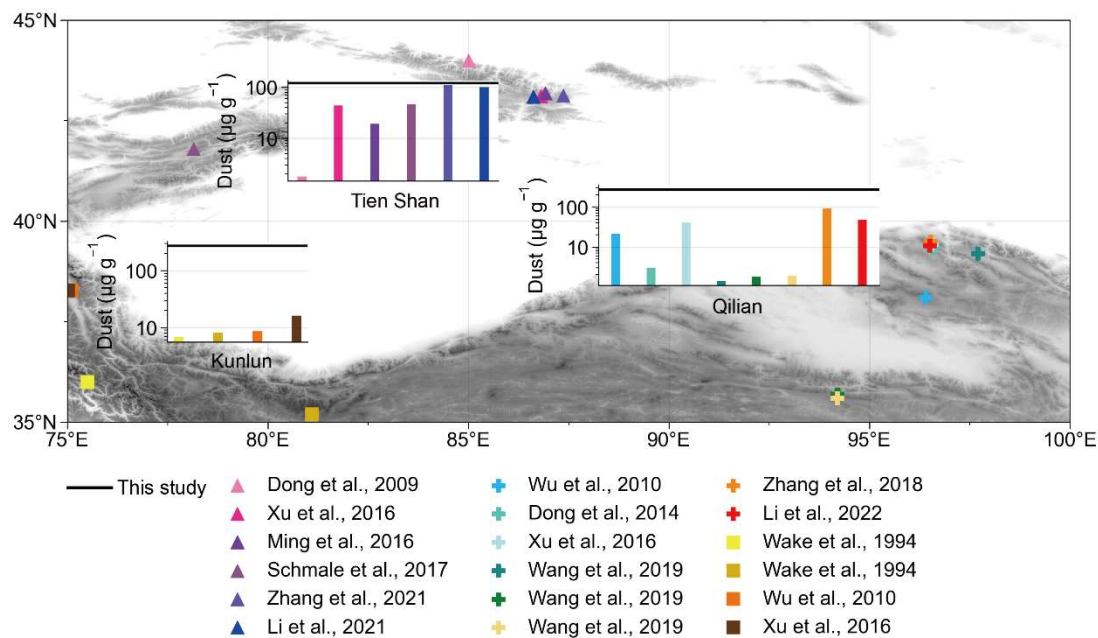
602 Scatter plots of the snow albedo reduction for the elevations across the Tien Shan,  
603 Kunlun Mountains, and Qilian Mountains are shown in Figure 11. The snow albedo  
604 reduction across the Tien Shan decreased with increasing elevation prior to the dust  
605 storm. However, the most severe dust deposition occurred within the 4000–4500 m  
606 elevation range, resulting in the most significant enhancement of snow albedo reduction  
607 in this elevation range. These findings are consistent with those reported for the  
608 Himalayas (Sarangi et al., 2020). The snow albedo reduction was generally low across  
609 the Kunlun Mountains for all of the elevation ranges. However, dust deposition caused  
610 the most significant albedo reduction within the 4500–5500 m elevation range, with a  
611 dramatic decrease of its influence above 6000 m. These findings correspond to the  
612 CALIPSO aerosol vertical profile observations (Figures 6j and k). The snow albedo  
613 reduction across the Qilian Mountains initially increased with elevation up to ~5000 m  
614 and then decreased at high elevations prior to the dust storm. However, the most severe  
615 dust deposition occurred across the lower elevations, leading to the most significant  
616 enhancement of snow albedo reduction across these lower-elevation regions. Our  
617 elevation analysis revealed a consistent outcome, whereby the dust storms significantly  
618 darkened the snowpack up to >5000 m elevation across the three analyzed mountain  
619 ranges.



620  
621 **Figure 11. Scatter plots of the snow albedo reductions for the analyzed elevation**  
622 **ranges across the (a) Tien Shan, (b) Kunlun Mountains, and (c) Qilian Mountains.**  
623 **Each box plot shows the statistical results for a 400-m elevation interval.**

624 **4 Discussion**

625 The snow darkening effect and its resultant radiative forcing have gained increasing  
626 attention in recent decades owing to their significant impacts on regional climate and  
627 hydrological systems. However, studies in the Tien Shan, Kunlun Mountains, and  
628 Qilian Mountains have been limited to local-scale observations, despite the significant  
629 impact of dust on snow darkening in these regions. Here we provide an overview of  
630 previous in situ dust-content measurements in the snowpack across the study region for  
631 comparison with our satellite remote-sensing results (see Figure 12). In the Tien Shan  
632 region, Ming et al. (2016), Xu et al. (2016), Li et al. (2021), and Zhang et al. (2021)  
633 reported a dust content of 19.3–110  $\mu\text{g g}^{-1}$  in the snowpack across Urumqi Glacier No.1.  
634 Dong et al. (2009) observed an average dust content of 0.97–3.69  $\mu\text{g g}^{-1}$  in the  
635 snowpack across Urumqi Glacier No. 1, Haxilegen Glacier No. 51, and Miaoergou  
636 Glacier. Schmale et al. (2017) found a variable dust content of 68.1–125.9  $\mu\text{g g}^{-1}$  in the  
637 snowpack across Suek Zapadniy, No. 354, and Golubin glaciers in the western Tien  
638 Shan. In the Kunlun Mountains, Wake et al. (1994) reported a dust content of up to ~8  
639  $\mu\text{g g}^{-1}$  in the snow/ice across the western Kunlun Mountains. Wu et al. (2010) and Xu  
640 et al. (2016) measured dust contents of ~8.68 and 16.24  $\mu\text{g g}^{-1}$  in the ice core and  
641 snowpack across Muztagata Glacier in the northwestern Tibet Plateau (Wu et al., 2010;  
642 Xu et al., 2016), respectively. In the Qilian Mountains, Wu et al. (2010) analyzed ice  
643 cores from Dunde Glacier and measured a dust content of ~21  $\mu\text{g g}^{-1}$ . The measured  
644 dust contents in the snowpack across Laohugou Glacier ranged from around 3 to 93.2  
645  $\mu\text{g g}^{-1}$  (Dong et al., 2014; Xu et al., 2016; Zhang et al., 2018; Li et al., 2022). Wang et  
646 al. (2019) measured a variable dust content of 1.4–1.9  $\mu\text{g g}^{-1}$  in the fresh snow across  
647 Qiyi, Meikuang, and Yuzhufeng glaciers. Overall, previous field studies have reported  
648 dust contents of 0.97–125.9, 6.78–16.24, and 1.4–93.2  $\mu\text{g g}^{-1}$  for the Tien Shan, Kunlun  
649 Mountains, and Qilian Mountains, respectively.



651

652

**Figure 12. Comparisons of the satellite-derived dust contents (black lines) in snow from this study and observed values from previous studies (colored symbols and bars).**

655 Our satellite-derived approach has yielded much higher dust contents than those  
 656 obtained via in situ field measurements, with 42–196, 170–360, and 194–360  $\mu\text{g g}^{-1}$   
 657 determined for the Tien Shan, Kunlun Mountains, and Qilian Mountains, respectively.  
 658 A key reason for this discrepancy could be that the field measurements usually record  
 659 the background dust content signal, which includes a gradual natural deposition of dust,  
 660 whereas our analysis specifically focused on significant snow darkening events due to  
 661 severe dust storms, which further highlights the advantage of employing remote-  
 662 sensing techniques to observe extreme snow darkening phenomena (Li et al., 2020).  
 663 We do note that satellite-derived approaches possess their own uncertainties, which  
 664 arise from the data resolution and accuracy, algorithm assumptions, and atmospheric  
 665 and underlying surface interferences (Cui et al., 2021). Nevertheless, this satellite-  
 666 derived approach remains a valuable tool for effectively and rapidly studying extreme  
 667 events, which cannot be captured by field measurements or climate model simulations,  
 668 particularly as these extreme events will become increasingly important for climate and  
 669 hydrological systems as the global climate continues to warm (Clow et al., 2016;  
 670 Dumont et al., 2020).

671 Given the significant snow darkening effect highlighted in this study and recent  
672 observations of decreasing snow cover across the Tien Shan, Kunlun Mountains, and  
673 Qilian Mountains (She et al., 2015; Li et al., 2020; Zhu et al., 2022), it is crucial to  
674 evaluate the impact of snow darkening on regional hydrologic cycles and local  
675 freshwater supplies. However, snow aging and melting mechanisms are complex and  
676 therefore require complementary observations because remote sensing alone cannot  
677 distinguish the influences of augmented shortwave radiation owing to dust and  
678 increased air temperatures on snow aging and melting (Gautam et al., 2013). Additional  
679 research that integrates model simulations and satellite observations is necessary to  
680 differentiate the roles of snow darkening and global warming in enhancing snow aging  
681 and melting, and the resultant changes in glacier runoff in the future.

682 **5 Conclusions**

683 Our study focused on the impact of the annual vast dust emissions from the Taklamakan  
684 Desert on the surrounding high mountain snowpack. Using a combination of MODIS  
685 satellite data analysis and SNICAR model simulations, we aimed to reveal significant  
686 snow-darkening events and quantify the resulting snow albedo reduction and radiative  
687 forcing caused by severe dust storms. Our analysis of the satellite data revealed  
688 significant snow darkening over the 3000–6000 m elevation range across the Tien Shan  
689 and Kunlun Mountains. This phenomenon was attributed to the high uplift of dust  
690 owing to the local topography and atmospheric circulation. The impacted area,  
691 spanning the track of the dust storm, encompassed almost all of the snow-covered areas  
692 across the Tien Shan ( $>2100 \text{ km}^2$ ) and Kunlun Mountains ( $>600 \text{ km}^2$ ), including the  
693 summits. The dust content in the snowpack increased to 42–192 and  $170\text{--}360 \mu\text{g g}^{-1}$ ,  
694 resulting in significant increases in snow albedo reduction (radiative forcing) of 0.028–  
695  $0.079 (11\text{--}31.5 \text{ W m}^{-2})$  and  $0.088\text{--}0.136 (31\text{--}49 \text{ W m}^{-2})$  across the Tien Shan and  
696 Kunlun Mountains, respectively. Additionally, the dust storms accelerated snow aging,  
697 as indicated by the growth of  $R_{\text{eff}}$ . Furthermore, the dust plumes from the Taklamakan  
698 Desert traveled eastward, depositing dust across much of the snow-covered area ( $>630$   
699  $\text{km}^2$ ) in the Qilian Mountains, where the dust content significantly increased to 194–

700  $360 \mu\text{g g}^{-1}$ , causing a considerable increase in snow albedo reduction (radiative forcing)  
701 of  $0.092\text{--}0.153$  ( $22\text{--}38 \text{ W m}^{-2}$ ). The spatial distribution of the snow-darkening effect  
702 varied across all three mountain ranges due to the uneven deposition of dust, with the  
703 most significant snow darkening observed in the high elevation range of  $4000\text{--}5500 \text{ m}$ .  
704 Moreover, by comparing our satellite-derived results with previous field measurements,  
705 we found that severe dust storms, occurring over short periods, have a more profound  
706 effect on snow darkening compared with the relatively slow deposition of dust in the  
707 absence of dust storms. These severe snow darkening events were not limited to the  
708 three typical cases but occurred widely (Figures S13-S21). This highlights the  
709 importance of satellite-derived analyses in capturing extreme dust deposition events  
710 that may be challenging to detect through field measurements and climate model  
711 simulations. Our findings underscore the significance of understanding the impact of  
712 dust deposition on snow albedo and radiative forcing for accurate assessment of the  
713 environmental effects of these extreme events.

714

715

716

717

718

719

720

721

722

723

724

725 *Data availability.* All datasets and codes used to produce this study can be obtained by  
726 contacting Wei Pu (puwei@lzu.edu.cn).

727 *Author contributions.* WP and XW designed the study and developed the overarching  
728 research goals and aims. YX carried the study out and wrote the first draft with  
729 contributions from all co-authors. YX processed the data with the assistance of YC, SY,  
730 TS, XC, XN, DW, JC and YZ. WP and XW assumed oversight and leadership  
731 responsibility for the research activity planning and execution. All authors contributed  
732 to the improvement of results and revised the final paper.

733 *Competing interests.* The authors declare that they have no conflict of interest.

734 *Acknowledgements.* The Lanzhou University group acknowledges support from the  
735 National Science Fund for Distinguished Young Scholars, the State Key Laboratory of  
736 Cryosphere Science Open Fund and the National Natural Science Foundation of China.  
737 We appreciate Dr. Boyuan Zhang's assistance with the code improvements. We thank  
738 Lanzhou City's scientific research funding subsidy to Lanzhou University and the  
739 Supercomputing Center of Lanzhou University for providing the computing services.

740 *Financial support.* This research was supported by the National Science Fund for  
741 Distinguished Young Scholars (42025102), the State Key Laboratory of Cryosphere  
742 Science Open Fund (SKLCS-OP-2021-05) and the National Natural Science  
743 Foundation of China (42375068 and 42075061) and the Natural Science Foundation of  
744 Gansu province, China (21ZDKA0017). We also appreciate the insightful comments  
745 provided by the editor and the two reviewers.

746 **Reference**

- 747 Arun, B. S., Aswini, A. R., Gogoi, M. M., Hegde, P., Kumar Kompalli, S., Sharma, P.,  
748 and Suresh Babu, S.: Physico-chemical and optical properties of aerosols at a  
749 background site (~4 km a.s.l.) in the western Himalayas, *Atmospheric*  
750 *Environment*, 218, 10.1016/j.atmosenv.2019.117017, 2019.
- 751 Arun, B. S., Gogoi, M. M., Borgohain, A., Hegde, P., Kundu, S. S., and Babu, S. S.:  
752 Role of sulphate and carbonaceous aerosols on the radiative effects of aerosols  
753 over a remote high-altitude site Lachung in the Eastern Himalayas, *Atmospheric*  
754 *Research*, 263, 10.1016/j.atmosres.2021.105799, 2021a.
- 755 Arun, B. S., Gogoi, M. M., Hegde, P., Borgohain, A., Boreddy, S. K. R., Kundu, S. S.,  
756 and Babu, S. S.: Carbonaceous Aerosols over Lachung in the Eastern Himalayas:  
757 Primary Sources and Secondary Formation of Organic Aerosols in a Remote High-  
758 Altitude Environment, *ACS Earth and Space Chemistry*, 5, 2493-2506,  
759 10.1021/acsearthspacechem.1c00190, 2021b.
- 760 Bair, E. H., Stillinger, T., and Dozier, J.: Snow property inversion from remote sensing  
761 (SPIReS): A generalized multispectral unmixing approach with examples from  
762 MODIS and Landsat 8 OLI, *IEEE Transactions on Geoscience and Remote*  
763 *Sensing*, 59, 7270-7284, 10.1109/tgrs.2020.3040328, 2020.
- 764 Baladima, F., Thomas, J. L., Voisin, D., Dumont, M., Junquas, C., Kumar, R., Lavaysse,  
765 C., Marelle, L., Parrington, M., and Flemming, J.: Modeling an extreme dust  
766 deposition event to the French Alpine seasonal snowpack in April 2018:  
767 Meteorological context and predictions of dust deposition, *Journal of Geophysical*  
768 *Research: Atmospheres*, 127, 10.1029/2021jd035745, 2022.
- 769 Bormann, K. J., Brown, R. D., Derksen, C., Painter, T. H.: Estimating snow-cover  
770 trends from space, *Nature Climate Change*, 11, 924-928, 10.1038/s41558-018-  
771 0318-3, 2018.
- 772 Chaubey, J. P., Moorthy, K. K., Babu, S. S., Nair, V. S., and Tiwari, A.: Black carbon  
773 aerosols over coastal Antarctica and its scavenging by snow during the Southern  
774 Hemispheric summer, *Journal of Geophysical Research: Atmospheres*, 115,  
775 10.1029/2009jd013381, 2010.
- 776 Chen, B., Song, Z., Huang, J., Zhang, P., Hu, X., Zhang, X., Guan, X., Ge, J., and Zhou,  
777 X.: Estimation of atmospheric PM10 Concentration in China using an  
778 interpretable deep learning model and top-of-the-atmosphere reflectance data from  
779 China's new generation geostationary meteorological satellite, FY-4A, *Journal of*  
780 *Geophysical Research: Atmospheres*, 127, 10.1029/2021jd036393, 2022.
- 781 Chen, S., Huang, J., Zhao, C., Qian, Y., Leung, L. R., and Yang, B.: Modeling the  
782 transport and radiative forcing of Taklimakan dust over the Tibetan Plateau: A case  
783 study in the summer of 2006, *Journal of Geophysical Research: Atmospheres*, 118,  
784 797-812, 10.1002/jgrd.50122, 2013.
- 785 Chen, S., Huang, J., Li, J., Jia, R., Jiang, N., Kang, L., Ma, X., and Xie, T.: Comparison  
786 of dust emissions, transport, and deposition between the Taklimakan Desert and  
787 Gobi Desert from 2007 to 2011, *Science China Earth Sciences*, 60, 1338-1355,  
788 10.1007/s11430-016-9051-0, 2017a.
- 789 Chen, S., Huang, J., Kang, L., Wang, H., Ma, X., He, Y., Yuan, T., Yang, B., Huang, Z.,

- 790 and Zhang, G.: Emission, transport, and radiative effects of mineral dust from the  
791 Taklimakan and Gobi deserts: comparison of measurements and model results,  
792 *Atmospheric Chemistry and Physics*, 17, 2401-2421, 10.5194/acp-17-2401-2017,  
793 2017b.
- 794 Chen, W., Wang, X., Cui, J., Cao, X., Pu, W., Zheng, X., Ran, H., and Ding, J.: Radiative  
795 forcing of black carbon in seasonal snow of wintertime based on remote sensing  
796 over Xinjiang, China, *Atmospheric Environment*, 247,  
797 10.1016/j.atmosenv.2021.118204, 2021.
- 798 Clow, D. W., Williams, M. W., and Schuster, P. F.: Increasing aeolian dust deposition to  
799 snowpacks in the Rocky Mountains inferred from snowpack, wet deposition, and  
800 aerosol chemistry, *Atmospheric Environment*, 146, 183-194,  
801 10.1016/j.atmosenv.2016.06.076, 2016.
- 802 Cohen, J. and Rind, D.: The Effect of Snow Cover on the Climate, *J. Climate*, 4, 689–  
803 706, 10.1175/1520-0442(1991)004<0689:Teosco>2.0.Co;2, 1991.
- 804 Copernicus Climate Change Service: ERA5: Fifth generation of ECMWF atmospheric  
805 reanalysis of the global climate, Copernicus Climate Change Service Climate Data  
806 Store (CDS), 2017.
- 807 Cordero, R., Sepúlveda, E., Feron, S., Damiani, A., Fernandoy, F., Neshyba, S., Rowe,  
808 P. M., Asencio, V., Carrasco, J., Alfonso, J. A., Llanillo, P., Wachter, P., Seckmeyer,  
809 G., Stepanova, M., Carrera, J. M., Jorquera, J., Wang, C., Malhotra, A., Dana, J.,  
810 Khan, A. L., and Casassa, G.: Black carbon footprint of human presence in  
811 Antarctica, *Nature Communications*, 13, 2041-1723, s41467-022-28560-w, 2022.
- 812 Cui, J., Shi, T., Zhou, Y., Wu, D., Wang, X., and Pu, W.: Satellite-based radiative forcing  
813 by light-absorbing particles in snow across the Northern Hemisphere,  
814 *Atmospheric Chemistry and Physics*, 21, 269-288, 10.5194/acp-21-269-2021,  
815 2021.
- 816 Cui, J., Niu, X., Chen, Y., Xing, Y., Yan, S., Zhao, J., Chen, L., Xu, S., Wu, D., Shi, T.,  
817 Wang, X., and Pu, W.: The Spatio-Temporal Variability in the Radiative Forcing  
818 of Light-Absorbing Particles in Snow of 2003–2018 over the Northern  
819 Hemisphere from MODIS, *Remote Sensing*, 15, 636, 10.3390/rs15030636, 2023.
- 820 Dang, C., Warren, S. G., Fu, Q., Doherty, S. J., Sturm, M., and Su, J.: Measurements of  
821 light-absorbing particles in snow across the Arctic, North America, and China:  
822 Effects on surface albedo, *Journal of Geophysical Research: Atmospheres*, 122,  
823 10.1002/2017jd027070, 2017.
- 824 Di Mauro, B., Fava, F., Ferrero, L., Garzonio, R., Baccolo, G., Delmonte, B., and  
825 Colombo, R.: Mineral dust impact on snow radiative properties in the European  
826 Alps combining ground, UAV, and satellite observations, *Journal of Geophysical  
827 Research: Atmospheres*, 120, 6080-6097, 10.1002/2015jd023287, 2015.
- 828 Dong, Z., Li, Z., Wang, F., and Zhang, M.: Characteristics of atmospheric dust  
829 deposition in snow on the glaciers of the eastern Tien Shan, China, *Journal of  
830 Glaciology*, 55, 797-804, 10.3189/002214309790152393, 2009.
- 831 Dong, Z., Qin, D., Chen, J., Qin, X., Ren, J., Cui, X., Du, Z., and Kang, S.:  
832 Physicochemical impacts of dust particles on alpine glacier meltwater at the  
833 Laohugou Glacier basin in western Qilian Mountains, China, *Science of the Total*

- 834 Environment, 493, 930-942, 10.1016/j.scitotenv.2014.06.025, 2014.
- 835 Dong, Z., Brahney, J., Kang, S., Elser, J., Wei, T., Jiao, X., and Shao, Y.: Aeolian dust  
836 transport, cycle and influences in high-elevation cryosphere of the Tibetan Plateau  
837 region: New evidences from alpine snow and ice, Earth-Science Reviews, 211,  
838 10.1016/j.earscirev.2020.103408, 2020.
- 839 Dong, Q., Huang, Z., Li, W., Li, Z., Song, X., Liu, W., Wang, T., Bi, J., and Shi, J.:  
840 Polarization lidar measurements of dust optical properties at the junction of the  
841 Taklimakan Desert–Tibetan Plateau, Remote Sensing, 14, 10.3390/rs14030558,  
842 2022.
- 843 Dumont, M., Brun, E., Picard, G., Michou, M., Libois, Q., Petit, J. R., Geyer, M., Morin,  
844 S., and Josse, B.: Contribution of light-absorbing impurities in snow to  
845 Greenland's darkening since 2009, Nature Geoscience, 7, 509-512,  
846 10.1038/ngeo2180, 2014.
- 847 Dumont, M., Tuzet, F., Gascoin, S., Picard, G., Kutuzov, S., Lafaysse, M., Cluzet, B.,  
848 Nheili, R., and Painter, T. H.: Accelerated snow melt in the Russian Caucasus  
849 Mountains after the Saharan dust outbreak in March 2018, Journal of Geophysical  
850 Research: Earth Surface, 125, 10.1029/2020jf005641, 2020.
- 851 Flanner, M. G., Zender, C. S., Randerson, J. T., and Rasch, P. J.: Present-day climate  
852 forcing and response from black carbon in snow, Journal of Geophysical Research,  
853 112, 10.1029/2006jd008003, 2007.
- 854 Flanner, M. G., Zender, C. S., Hess, P. G., Mahowald, N. M., Painter, T. H., Ramanathan,  
855 V., and Rasch, P. J.: Springtime warming and reduced snow cover from  
856 carbonaceous particles, Atmospheric Chemistry and Physics., 9, 2481–2497,  
857 10.5194/acp-9-2481-2009, 2009.
- 858 Flanner, M. G., Arnheim, J. B., Cook, J. M., Dang, C., He, C., Huang, X., Singh, D.,  
859 Skiles, S. M., Whicker, C. A., and Zender, C. S.: SNICAR-ADv3: a community  
860 tool for modeling spectral snow albedo, Geoscientific Model Development, 14,  
861 7673-7704, 10.5194/gmd-14-7673-2021, 2021.
- 862 Gautam, R., Hsu, N. C., Lau, W. K. M., and Yasunari, T. J.: Satellite observations of  
863 desert dust-induced Himalayan snow darkening, Geophysical Research Letters, 40,  
864 988-993, 10.1002/grl.50226, 2013.
- 865 Ge, J. M., Huang, J. P., Xu, C. P., Qi, Y. L., and Liu, H. Y.: Characteristics of Taklimakan  
866 dust emission and distribution: A satellite and reanalysis field perspective, Journal  
867 of Geophysical Research: Atmospheres, 119, 11,772-711,783,  
868 10.1002/2014jd022280, 2014.
- 869 Gogoi, M. M., Babu, S. S., Pandey, S. K., Nair, V. S., Vaishya, A., Girach, I. A., and  
870 Koushik, N.: Scavenging ratio of black carbon in the Arctic and the Antarctic,  
871 Polar Science, 16, 10-22, 10.1016/j.polar.2018.03.002, 2018.
- 872 Gogoi M. M., Babu, S. S., Arun, B. S., Moorthy, K. K., Ajay, A., Ajay, P., Suryavanshi,  
873 A., Borgohain, A., Guha, A., Shaikh, A., Pathak, B., Gharai, B., Ramasamy, B.,  
874 Balakrishnaiah, G., Menon, H. B., Kuniyal, J. C., Krishnan, J., Gopal, K. R.,  
875 Maheswari, M., Naja, M., Kaur, P., Bhuyan, P. K., Gupta, P., Singh, P., Srivastava,  
876 P., Singh, R. S., Kumar, R., Rastogi, S., Kundu, S. S., Kompalli, S. K., Panda, S.,  
877 Rao, T. C., Das, T., and Kant, Y.: Response of ambient BC concentration across

- 878 the Indian region to the nation-wide lockdown: results from the ARFINET  
879 measurements of ISRO-GBP, *Current Science*, 120, 10.18520/cs/v120/i2/341-351,  
880 2021a.
- 881 Gogoi, M. M., Pandey, S. K., Arun, B. S., Nair, V. S., Thakur, R. C., Chaubey, J. P.,  
882 Tiwari, A., Manoj, M. R., Kompalli, S. K., Vaishya, A., Prijith, S. S., Hegde, P.,  
883 and Babu, S. S.: Long-term changes in aerosol radiative properties over Ny-  
884 Ålesund: Results from Indian scientific expeditions to the Arctic, *Polar Science*,  
885 30, 10.1016/j.polar.2021.100700, 2021b.
- 886 Gui, K., Yao, W., Che, H., An, L., Zheng, Y., Li, L., Zhao, H., Zhang, L., Zhong, J.,  
887 Wang, Y., and Zhang, X.: Record-breaking dust loading during two mega dust  
888 storm events over northern China in March 2021: aerosol optical and radiative  
889 properties and meteorological drivers, *Atmospheric Chemistry and Physics*, 22,  
890 7905-7932, 10.5194/acp-22-7905-2022, 2022.
- 891 Hadley, O. L. and Kirchstetter, T. W.: Black-carbon reduction of snow albedo, *Nat. Clim.  
892 Change*, 2, 437–440, 10.1038/nclimate1433, 2012.
- 893 Han, Y., Wang, T., Tang, J., Wang, C., Jian, B., Huang, Z., and Huang, J.: New insights  
894 into the Asian dust cycle derived from CALIPSO lidar measurements, *Remote  
895 Sensing of Environment*, 272, 10.1016/j.rse.2022.112906, 2022.
- 896 He, C., Takano, Y., Liou, K.-N., Yang, P., Li, Q., and Chen, F.: Impact of snow grain  
897 shape and black carbon–snow internal mixing on snow optical properties:  
898 Parameterizations for climate models, *Journal of Climate*, 30, 10019-10036,  
899 10.1175/jcli-d-17-0300.1, 2017.
- 900 He, C., Liou, K. N., Takano, Y., Yang, P., Qi, L., and Chen, F.: Impact of grain shape  
901 and multiple black carbon internal mixing on snow albedo: Parameterization and  
902 radiative effect analysis, *Journal of Geophysical Research: Atmospheres*, 123,  
903 1253-1268, 10.1002/2017jd027752, 2018.
- 904 Huang, H., Qian, Y., He, C., Bair, E. H., and Rittger, K.: Snow albedo feedbacks  
905 enhance snow impurity-induced radiative forcing in the Sierra Nevada,  
906 *Geophysical Research Letters*, 49, e2022GL098102, 10.1029/2022GL098102,  
907 2022.
- 908 Huang, J., Minnis, P., Yi, Y., Tang, Q., Wang, X., Hu, Y., Liu, Z., Ayers, K., Trepte, C.,  
909 and Winker, D.: Summer dust aerosols detected from CALIPSO over the Tibetan  
910 Plateau, *Geophysical Research Letters*, 34, 10.1029/2007gl029938, 2007.
- 911 Huang, J., Minnis, P., Chen, B., Huang, Z., Liu, Z., Zhao, Q., Yi, Y., and Ayers, J. K.:  
912 Long-range transport and vertical structure of Asian dust from CALIPSO and  
913 surface measurements during PACDEX, *Journal of Geophysical Research*, 113,  
914 10.1029/2008jd010620, 2008.
- 915 Huang, J., Wang, T., Wang, W., Li, Z., and Yan, H.: Climate effects of dust aerosols  
916 over East Asian arid and semiarid regions, *Journal of Geophysical Research: Atmospheres*, 119, 10.1002/2014jd021796, 2014.
- 917 Immerzeel, W. W. and Bierkens, M. F. P.: Asia's water balance, *Nature Geoscience*, 5,  
918 841-842, 10.1038/ngeo1643, 2012.
- 919 Jia, R., Liu, Y., Chen, B., Zhang, Z., and Huang, J.: Source and transportation of summer  
920 dust over the Tibetan Plateau, *Atmospheric Environment*, 123, 210-219,

- 922 10.1016/j.atmosenv.2015.10.038, 2015.
- 923 Kang, L., Huang, J., Chen, S., and Wang, X.: Long-term trends of dust events over  
924 Tibetan Plateau during 1961–2010, *Atmospheric Environment*, 125, 188-198,  
925 10.1016/j.atmosenv.2015.10.085, 2016.
- 926 Kraaijenbrink, P. D. A., Bierkens, M. F. P., Lutz, A. F., and Immerzeel, W. W.: Impact  
927 of a global temperature rise of 1.5 degrees Celsius on Asia's glaciers, *Nature*, 549,  
928 257-260, 10.1038/nature23878, 2017.
- 929 Kraaijenbrink, P. D. A., Stigter, E. E., Yao, T., and Immerzeel, W. W.: Climate change  
930 decisive for Asia's snow meltwater supply, *Nature Climate Change*, 11, 591-597,  
931 10.1038/s41558-021-01074-x, 2021.
- 932 Li, Y., Chen, Y., and Li, Z.: Climate and topographic controls on snow phenology  
933 dynamics in the Tianshan Mountains, Central Asia, *Atmospheric Research*, 236,  
934 10.1016/j.atmosres.2019.104813, 2020.
- 935 Li, Y., Kang, S., Zhang, X., Chen, J., Schmale, J., Li, X., Zhang, Y., Niu, H., Li, Z., Qin,  
936 X., He, X., Yang, W., Zhang, G., Wang, S., Shao, L., and Tian, L.: Black carbon  
937 and dust in the Third Pole glaciers: Reevaluated concentrations, mass absorption  
938 cross-sections and contributions to glacier ablation, *Science of the Total  
939 Environment*, 789, 147746, 10.1016/j.scitotenv.2021.147746, 2021.
- 940 Li, Y., Kang, S., Zhang, X., Li, C., Chen, J., Qin, X., Shao, L., and Tian, L.: Dust  
941 dominates the summer melting of glacier ablation zones on the northeastern  
942 Tibetan Plateau, *Science of the Total Environment*, 856, 159214,  
943 10.1016/j.scitotenv.2022.159214, 2022.
- 944 Liang, P., Chen, B., Yang, X., Liu, Q., Li, A., Mackenzie, L., and Zhang, D.: Revealing  
945 the dust transport processes of the 2021 mega dust storm event in northern China,  
946 *Science Bulletin*, 67, 21-24, 10.1016/j.scib.2021.08.014, 2021.
- 947 Ménégoz, M., Krinner, G., Balkanski, Y., Boucher, O., Cozic, A., Lim, S., Ginot, P., Laj,  
948 P., Gallée, H., Wagnon, P., Marinoni, A., and Jacobi, H. W.: Snow cover sensitivity  
949 to black carbon deposition in the Himalayas: from atmospheric and ice core  
950 measurements to regional climate simulations, *Atmospheric Chemistry and  
951 Physics*, 14, 4237-4249, 10.5194/acp-14-4237-2014, 2014.
- 952 Meng, L., Yang, X., Zhao, T., He, Q., Lu, H., Mamtimin, A., Huo, W., Yang, F., and Liu,  
953 C.: Modeling study on three-dimensional distribution of dust aerosols during a  
954 dust storm over the Tarim Basin, Northwest China, *Atmospheric Research*, 218,  
955 285-295, 10.1016/j.atmosres.2018.12.006, 2018.
- 956 Ming, J., Xiao, C. D., Wang, F. T., Li, Z. Q., and Li, Y. M.: Grey Tianshan Urumqi  
957 Glacier No.1 and light-absorbing impurities, *Environmental Science and Pollution  
958 Research*, 23, 9549-9558, 10.1007/s11356-016-6182-7, 2016.
- 959 Mishra, S. K., Hayse, J., Veselka, T., Yan, E., Kayastha, R. B., LaGory, K., McDonald,  
960 K., and Steiner, N.: An integrated assessment approach for estimating the  
961 economic impacts of climate change on River systems: An application to  
962 hydropower and fisheries in a Himalayan River, Trishuli, *Environmental Science  
963 & Policy*, 87, 102-111, 10.1016/j.envsci.2018.05.006, 2018.
- 964 Mishra, S. K., Rupper, S., Kapnick, S., Casey, K., Chan, H. G., Ciraci, E., Haritashya,  
965 U., Hayse, J., Kargel, J. S., Kayastha, R. B., Krakauer, N. Y., Kumar, S. V.,

- 966 Lammers, R. B., Maggioni, V., Margulis, S. A., Olson, M., Osmanoglu, B., Qian,  
967 Y., McLarty, S., Rittger, K., Rounce, D. R., Shean, D., Velicogna, I., Veselka, T.  
968 D., and Arendt, A.: Grand challenges of hydrologic modeling for food-energy-  
969 water nexus security in High Mountain Asia, *Frontiers in Water*, 3,  
970 10.3389/frwa.2021.728156, 2021.
- 971 Negi, H. S. and Kokhanovsky, A.: Retrieval of snow grain size and albedo of western  
972 Himalayan snow cover using satellite data, *The Cryosphere*, 5, 831-847,  
973 10.5194/tc-5-831-2011, 2011.
- 974 Notarnicola, C.: Hotspots of snow cover changes in global mountain regions over  
975 2000–2018, *Remote Sensing of Environment*, 243, 111781,  
976 10.1016/j.rse.2020.111781, 2020.
- 977 Niu, X., Pu, W., Fu, P., Chen, Y., Xing, Y., Wu, D., Chen, Z., Shi, T., Zhou, Y., Wen, H.,  
978 and Wang, X.: Fluorescence characteristics, absorption properties, and radiative  
979 effects of water-soluble organic carbon in seasonal snow across northeastern China,  
980 *Atmospheric Chemistry and Physics*, 22, 14075-14094, 10.5194/acp-22-14075-  
981 2022, 2022.
- 982 Okada, K., Kai, K: Atmospheric mineral particles collected at Qira in the Taklamakan  
983 Desert, China, *Atmospheric Environment*, 38, 6927-6935,  
984 10.1016/j.atmosenv.2004.03.078, 2004.
- 985 Orsolini, Y., Wegmann, M., Dutra, E., Liu, B., Balsamo, G., Yang, K., de Rosnay, P.,  
986 Zhu, C., Wang, W., Senan, R., and Arduini, G.: Evaluation of snow depth and snow  
987 cover over the Tibetan Plateau in global reanalyses using in situ and satellite  
988 remote sensing observations, *The Cryosphere*, 13, 2221-2239, 10.5194/tc-13-  
989 2221-2019, 2019.
- 990 Painter, T. H., Rittger, K., McKenzie, C., Slaughter, P., Davis, R. E., and Dozier, J.:  
991 Retrieval of subpixel snow covered area, grain size, and albedo from MODIS,  
992 *Remote Sensing of Environment*, 113, 868-879, 10.1016/j.rse.2009.01.001, 2009.
- 993 Painter, T. H., Bryant, A. C., and Skiles, S. M.: Radiative forcing by light absorbing  
994 impurities in snow from MODIS surface reflectance data, *Geophysical Research  
995 Letters*, 39, n/a-n/a, 10.1029/2012gl052457, 2012.
- 996 Painter, T. H., Skiles, S. M., Deems, J. S., Brandt, W. T., and Dozier, J.: Variation in  
997 rising limb of colorado river snowmelt runoff hydrograph controlled by dust  
998 radiative forcing in snow, *Geophysical Research Letters*, 45, 797-808,  
999 10.1002/2017gl075826, 2017.
- 1000 Patterson, E.M.: Optical properties of the crustal aerosol: Relation to chemical and  
1001 physical characteristics, *Journal of Geophysical Research: Atmospheres*, 86, 3236-  
1002 3246, 10.1029/JC086iC04p03236, 1981.
- 1003 Pu, W., Wang, X., Wei, H., Zhou, Y., Shi, J., Hu, Z., Jin, H., and Chen, Q.: Properties  
1004 of black carbon and other insoluble light-absorbing particles in seasonal snow of  
1005 northwestern China, *The Cryosphere*, 11, 1213–1233, 10.5194/tc-11-1213-2017,  
1006 2017.
- 1007 Pu, W., Cui, J., Shi, T., Zhang, X., He, C., and Wang, X.: The remote sensing of radiative  
1008 forcing by light-absorbing particles (LAPs) in seasonal snow over northeastern  
1009 China, *Atmospheric Chemistry and Physics*, 19, 9949-9968, 10.5194/acp-19-

- 1010 9949-2019, 2019.
- 1011 Pu, W., Cui, J., Wu, D., Shi, T., Chen, Y., Xing, Y., Zhou, Y., and Wang, X.:  
1012 Unprecedented snow darkening and melting in New Zealand due to 2019–2020  
1013 Australian wildfires, Fundamental Research, 1, 224-231,  
1014 10.1016/j.fmre.2021.04.001, 2021.
- 1015 Pulliainen, J., Luojus, K., Derksen, C., Mudryk, L., Lemmetyinen, J., Salminen, M.,  
1016 Ikonen, J., Takala, M., Cohen, J., Smolander, T., and Norberg, J.: Patterns and  
1017 trends of Northern Hemisphere snow mass from 1980 to 2018, 581, 294-298,  
1018 s41586-020-2258-0, 2020.
- 1019 Qian, Y., Yasunari, T. J., Doherty, S. J., Flanner, M. G., Lau, W. K. M., Ming, J., Wang,  
1020 H., Wang, M., Warren, S. G., and Zhang, R.: Light-absorbing particles in snow and  
1021 ice: Measurement and modeling of climatic and hydrological impact, Advances in  
1022 Atmospheric Sciences, 32, 64-91, 10.1007/s00376-014-0010-0, 2015.
- 1023 Qiu, X., Zeng, Y., and Miao, Q.: Sand-dust storms in China: temporal-spatial  
1024 distribution and tracks of source lands, Journal of Geographical Sciences. 11, 253–  
1025 260, 10.1007/BF02892308, 2001.
- 1026 Reveillet, M., Dumont, M., Gascoin, S., Lafaysse, M., Nabat, P., Ribes, A., Nheili, R.,  
1027 Tuzet, F., Menegoz, M., Morin, S., Picard, G., and Ginoux, P.: Black carbon and  
1028 dust alter the response of mountain snow cover under climate change, Nature  
1029 Communication, 13, 5279, 10.1038/s41467-022-32501-y, 2022.
- 1030 Ricchiazzi, P., Yang, S. R., Gautier, C., and Sowle, D.: SBDART: A research and  
1031 teaching software tool for plane-parallel radiative transfer in the Earth's  
1032 atmosphere, Bulletin of the American Meteorological Society., 79, 2101–2114,  
1033 10.1175/1520-0477(1998)079<2101:Sarats>2.0.Co;2, 1998.
- 1034 Rittger, K., Painter, T. H., and Dozier, J.: Assessment of methods for mapping snow  
1035 cover from MODIS, Advances in Water Resources, 51, 367-380,  
1036 10.1016/j.advwatres.2012.03.002, 2013.
- 1037 Rohde, A., Vogel, H., Hoshayaripour, H. A., Kottmeier C., and Vogel, B.: Regional  
1038 Impact of Snow-Darkening on Snow Pack and the Atmosphere During a Severe  
1039 Saharan Dust Deposition Event in Eurasia, Journal of Geophysical Research: Earth  
1040 Surface, 128, 10.1029/2022JF007016, 2023.
- 1041 Roychoudhury, C., He, C., Kumar, R., McKinnon, J. M., and Arellano, A. F.: On the  
1042 relevance of aerosols to snow cover variability over High Mountain Asia,  
1043 Geophysical Research Letters, 49, 10.1029/2022gl099317, 2022.
- 1044 Sang, J., Kim, M.-K., Lau, W. K. M., and Kim, K.-M.: Possible Impacts of snow  
1045 darkening effects on the hydrological cycle over western Eurasia and east Asia,  
1046 Atmosphere, 10, 10.3390/atmos10090500, 2019.
- 1047 Sarangi, C., Qian, Y., Rittger, K., Bormann, K. J., Liu, Y., Wang, H., Wan, H., Lin, G.,  
1048 and Painter, T. H.: Impact of light-absorbing particles on snow albedo darkening  
1049 and associated radiative forcing over high-mountain Asia: high-resolution WRF-  
1050 Chem modeling and new satellite observations, Atmospheric Chemistry and  
1051 Physics, 19, 7105-7128, 10.5194/acp-19-7105-2019, 2019.
- 1052 Sarangi, C., Qian, Y., Rittger, K., Ruby Leung, L., Chand, D., Bormann, K. J., and  
1053 Painter, T. H.: Dust dominates high-altitude snow darkening and melt over high-

- 1054 mountain Asia, *Nature Climate Change*, 10, 1045-1051, 10.1038/s41558-020-  
1055 00909-3, 2020.
- 1056 Schmale, J., Flanner, M., Kang, S. C., Sprenger, M., Zhang, Q. G., Guo, J. M., Li, Y.,  
1057 Schwikowski, M., and Farinotti, D.: Modulation of snow reflectance and  
1058 snowmelt from Central Asian glaciers by anthropogenic black carbon, *Scientific  
1059 Reports*, 7, 40501, 10.1038/srep40501, 2017.
- 1060 Siegmund., A. and Menz., G.: Fernes nah gebracht – satelliten- und luftbildeinsatz zur  
1061 analyse von umweltveränderungen im geographieunterricht, *Geographie und  
1062 Schule*, 154, 2–10, 2005.
- 1063 Shao, Y. and Dong, C. H.: A review on East Asian dust storm climate, modelling and  
1064 monitoring, *Global and Planetary Change*, 52, 1-22,  
1065 10.1016/j.gloplacha.2006.02.011, 2006.
- 1066 She, J., Zhang, Y., Li, X., and Feng, X.: Spatial and temporal characteristics of snow  
1067 cover in the Tizinafu watershed of the Western Kunlun Mountains, *Remote  
1068 Sensing*, 7, 3426-3445, 10.3390/rs70403426, 2015.
- 1069 Shi, T., Pu, W., Zhou, Y., Cui, J., Zhang, D., and Wang, X.: Albedo of black carbon-  
1070 contaminated snow across Northwestern China and the validation with model  
1071 simulation, *Journal of Geophysical Research: Atmospheres*, 125,  
1072 10.1029/2019jd032065, 2020.
- 1073 Shi, T., Cui, J., Chen, Y., Zhou, Y., Pu, W., Xu, X., Chen, Q., Zhang, X., and Wang, X.:  
1074 Enhanced light absorption and reduced snow albedo due to internally mixed  
1075 mineral dust in grains of snow, *Atmospheric Chemistry and Physics*, 21, 6035-  
1076 6051, 10.5194/acp-21-6035-2021, 2021.
- 1077 Shi, T., Cui, J., Wu, D., Xing, Y., Chen, Y., Zhou, Y., Pu, W., and Wang, X.: Snow albedo  
1078 reductions induced by the internal/external mixing of black carbon and mineral  
1079 dust, and different snow grain shapes across northern China, *Environmental  
1080 Research*, 208, 112670, 10.1016/j.envres.2021.112670, 2022a.
- 1081 Shi, T., Chen, Y., Xing, Y., Niu, X., Wu, D., Cui, J., Zhou, Y., Pu, W., and Wang, X.:  
1082 Assessment of the combined radiative effects of black carbon in the atmosphere  
1083 and snowpack in the Northern Hemisphere constrained by surface observations,  
1084 *Environmental Science: Atmospheres*, 2, 702-713, 10.1039/d2ea00005a, 2022b.
- 1085 Shi, T., He, C., Zhang, D., Zhang, X., Niu, X., Xing, Y., Chen, Y., Cui, J., Pu, W., and  
1086 Wang, X.: Opposite Effects of Mineral Dust Nonsphericity and Size on Dust-  
1087 Induced Snow Albedo Reduction, *Geophysical Research Letters*, 49,  
1088 10.1029/2022GL099031, 2022c.
- 1089 Shi, Z., Xie, X., Li, X., Yang, L., Xie, X., Lei, J., Sha, Y., and Liu, X.: Snow-darkening  
1090 versus direct radiative effects of mineral dust aerosol on the Indian summer  
1091 monsoon onset: role of temperature change over dust sources, *Atmospheric  
1092 Chemistry and Physics*, 19, 1605-1622, 10.5194/acp-19-1605-2019, 2019.
- 1093 Skiles, S. M. and Painter, T.: Daily evolution in dust and black carbon content, snow  
1094 grain size, and snow albedo during snowmelt, Rocky Mountains, Colorado,  
1095 *Journal of Glaciology*, 63, 118-132, 10.1017/jog.2016.125, 2016.
- 1096 Skiles, S. M., Flanner, M., Cook, J. M., Dumont, M., and Painter, T. H.: Radiative  
1097 forcing by light-absorbing particles in snow, *Nature Climate Change*, 8, 964-971,

- 1098 10.1038/s41558-018-0296-5, 2018a.
- 1099 Skiles, S. M., Mallia, D. V., Hallar, A. G., Lin, J. C., Lambert, A., Petersen, R., and  
1100 Clark, S.: Implications of a shrinking Great Salt Lake for dust on snow deposition  
1101 in the Wasatch Mountains, UT, as informed by a source to sink case study from  
1102 the 13–14 April 2017 dust event, *Environmental Research Letters*, 13,  
1103 10.1088/1748-9326/aaefd8, 2018b.
- 1104 Sun, J., Zhang, M., and Liu, T.: Spatial and temporal characteristics of dust storms in  
1105 China and its surrounding regions, 1960–1999: Relations to source area and  
1106 climate, *Journal of Geophysical Research: Atmospheres*, 106, 10325–10333,  
1107 10.1029/2000jd900665, 2001.
- 1108 Tang, W., Dai, T., Cheng, Y., Wang, S., and Liu, Y.: A study of a severe spring dust event  
1109 in 2021 over east Asia with WRF-Chem and multiple platforms of observations,  
1110 *Remote Sensing*, 14, 10.3390/rs14153795, 2022.
- 1111 Teillet, P. M., Guindon, B., and Goodenough, D. G.: On the slope-aspect correction of  
1112 multispectral scanner data, *Canadian Journal of Remote Sensing*, 8, 84–106,  
1113 10.1080/07038992.1982.10855028, 1982.
- 1114 Thakur, R. C., Arun, B. S., Gogoi, M. M., Thamban, M., Thayyen, R. J., Redkar, B. L.,  
1115 and Suresh Babu, S.: Multi-layer distribution of Black Carbon and inorganic ions  
1116 in the snowpacks of western Himalayas and snow albedo forcing, *Atmospheric  
1117 Environment*, 261, 10.1016/j.atmosenv.2021.118564, 2021.
- 1118 Usha, K. H., Nair, V. S., and Babu, S. S.: Deciphering the role of aerosol-induced snow  
1119 albedo feedback on dust emission over the Tibetan Plateau, *Journal of Geophysical  
1120 Research: Atmospheres*, 127, 10.1029/2021jd036384, 2022.
- 1121 Wake, C. P., Mayewski, P. A., Li, Z., Han, J., and Qin, D.: Modern eolian dust deposition  
1122 in central Asia, *Tellus B: Chemical and Physical Meteorology*, 46,  
1123 10.3402/tellusb.v46i3.15793, 1994.
- 1124 Wang, X., Huang, J., Ji, M., and Higuchi, K.: Variability of East Asia dust events and  
1125 their long-term trend, *Atmospheric Environment*, 42, 3156–3165,  
1126 10.1016/j.atmosenv.2007.07.046, 2008.
- 1127 Wang, X., Doherty, S. J., and Huang, J.: Black carbon and other light-absorbing  
1128 impurities in snow across Northern China, *Journal of Geophysical Research: Atmospheres*, 118, 1471–1492, 10.1029/2012jd018291, 2013.
- 1129 Wang, X., Pu, W., Ren, Y., Zhang, X., Zhang, X., Shi, J., Jin, H., Dai, M., and Chen, Q.:  
1130 Observations and model simulations of snow albedo reduction in seasonal snow  
1131 due to insoluble light-absorbing particles during 2014 Chinese survey,  
1132 *Atmospheric Chemistry and Physics*, 17, 2279–2296, 10.5194/acp-17-2279-2017,  
1133 2017.
- 1134 Wang, X., Wei, H., Liu, J., Xu, B., Wang, M., Ji, M., and Jin, H.: Quantifying the light  
1135 absorption and source attribution of insoluble light-absorbing particles on Tibetan  
1136 Plateau glaciers between 2013 and 2015, *The Cryosphere*, 13, 309–324,  
1137 10.5194/tc-13-309-2019, 2019.
- 1138 Wei, T., Dong, Z., Kang, S., Qin, X., and Guo, Z.: Geochemical evidence for sources  
1139 of surface dust deposited on the Laohugou glacier, Qilian Mountains, *Applied  
1140 Geochemistry*, 79, 1–8, 10.1016/j.apgeochem.2017.01.024, 2017.
- 1141

- 1142 Wiscombe, W. J. and Warren, S. G.: A model for the spectral albedo of snow .1. Pure  
1143 snow, *Journal of the Atmospheric Sciences*, 37, 2712–2733,  
1144 10.1175/15200469(1980)037<2712:Amftsa>2.0.Co;2, 1980.
- 1145 Wu, D., Liu, J., Wang, T., Niu, X., Chen, Z., Wang, D., Zhang, X., Ji, M., Wang, X.,  
1146 and Pu, W.: Applying a dust index over North China and evaluating the  
1147 contribution of potential factors to its distribution, *Atmospheric Research*, 254,  
1148 10.1016/j.atmosres.2021.105515, 2021.
- 1149 Wu, G., Yao, T., Xu, B., Tian, L., Zhang, C., and Zhang, X.: Dust concentration and  
1150 flux in ice cores from the Tibetan Plateau over the past few decades, *Tellus B: Chemical and Physical Meteorology*, 62, 10.1111/j.1600-0889.2010.00457.x,  
1151 2010.
- 1152 Xu, J., Kang, S., Hou, S., Zhang, Q., Huang, J., Xiao, C., Ren, J., and Qin, D.:  
1153 Characterization of contemporary aeolian dust deposition on mountain glaciers of  
1154 western China, *Sci. Cold Arid Reg*, 8, 0009-0021, 2016.
- 1155 Yang, L., Shi, Z., Xie, X., Li, X., Liu, X., and An, Z.: Seasonal changes in East Asian  
1156 monsoon-westerly circulation modulated by the snow-darkening effect of mineral  
1157 dust, *Atmospheric Research*, 279, 10.1016/j.atmosres.2022.106383, 2022.
- 1158 Yao, T., Thompson, L., Yang, W., Yu, W., Gao, Y., Guo, X., Yang, X., Duan, K., Zhao,  
1159 H., Xu, B., Pu, J., Lu, A., Xiang, Y., Kattel, D. B., and Joswiak, D.: Different  
1160 glacier status with atmospheric circulations in Tibetan Plateau and surroundings,  
1161 *Nature Climate Change*, 2, 663-667, 10.1038/nclimate1580, 2012.
- 1162 Yao, T., Xue, Y., Chen, D., Chen, F., Thompson, L., Cui, P., Koike, T., Lau, W. K. M.,  
1163 Lettenmaier, D., Mosbrugger, V., Zhang, R., Xu, B., Dozier, J., Gillespie, T., Gu,  
1164 Y., Kang, S., Piao, S., Sugimoto, S., Ueno, K., Wang, L., Wang, W., Zhang, F.,  
1165 Sheng, Y., Guo, W., Ailikun, Yang, X., Ma, Y., Shen, S. S. P., Su, Z., Chen, F.,  
1166 Liang, S., Liu, Y., Singh, V. P., Yang, K., Yang, D., Zhao, X., Qian, Y., Zhang, Y.,  
1167 and Li, Q.: Recent Third Pole's rapid warming accompanies cryospheric melt and  
1168 water cycle intensification and interactions between monsoon and environment:  
1169 Multidisciplinary approach with observations, modeling, and analysis, *Bulletin of  
1170 the American Meteorological Society*, 100, 423-444, 10.1175/bams-d-17-0057.1,  
1171 2019.
- 1172 Yuan, T., Chen, S., Huang, J., Wu, D., Lu, H., Zhang, G., Ma, X., Chen, Z., Luo, Y., and  
1173 Ma, X.: Influence of dynamic and thermal forcing on the meridional transport of  
1174 Taklimakan desert dust in spring and summer, *Journal of Climate*, 32, 749-767,  
1175 10.1175/jcli-d-18-0361.1, 2018.
- 1176 Zege, E. P., Katsev, I. L., Malinka, A. V., Prikhach, A. S., Heygster, G., and Wiebe, H.:  
1177 Algorithm for retrieval of the effective snow grain size and pollution amount from  
1178 satellite measurements, *Remote Sensing of Environment*, 115, 2674-2685,  
1179 10.1016/j.rse.2011.06.001, 2011.
- 1180 Zhang, B., Tsunekawa, A., and Tsubo, M.: Contributions of sandy lands and stony  
1181 deserts to long-distance dust emission in China and Mongolia during 2000–2006,  
1182 *Global and Planetary Change*, 60, 487-504, 10.1016/j.gloplacha.2007.06.001,  
1183 2008.
- 1184 Zhang, X., Li, Z. Q., You, X. N., She, Y. Y., Song, M. Y., and Zhou, X.: Light-Absorbing

- 1186        Impurities on Urumqi Glacier No.1 in Eastern Tien Shan: Concentrations and  
1187        Implications for Radiative Forcing Estimates During the Ablation Period,  
1188        *Frontiers in Earth Science*, 9, 2296-6463, 10.3389/feart.2021.524963, 2021.
- 1189        Zhang, Y., Kang, S., Sprenger, M., Cong, Z., Gao, T., Li, C., Tao, S., Li, X., Zhong, X.,  
1190        Xu, M., Meng, W., Neupane, B., Qin, X., and Sillanpää, M.: Black carbon and  
1191        mineral dust in snow cover on the Tibetan Plateau, *The Cryosphere*, 12, 413-431,  
1192        10.5194/tc-12-413-2018, 2018.
- 1193        Zhang, Y., Gao, T., Kang, S., Sprenger, M., Tao, S., Du, W., Yang, J., Wang, F., and  
1194        Meng, W.: Effects of black carbon and mineral dust on glacial melting on the Muz  
1195        Taw glacier, Central Asia, *Science of the Total Environment*, 740, 140056,  
1196        10.1016/j.scitotenv.2020.140056, 2020.
- 1197        Zhang, Y., Gao, T., Kang, S., Shangguan, D., and Luo, X.: Albedo reduction as an  
1198        important driver for glacier melting in Tibetan Plateau and its surrounding areas,  
1199        *Earth-Science Reviews*, 220, 10.1016/j.earscirev.2021.103735, 2021.
- 1200        Zhao, X., Huang, K., Fu, J. S., and Abdullaev, S. F.: Long-range transport of Asian dust  
1201        to the Arctic: identification of transport pathways, evolution of aerosol optical  
1202        properties, and impact assessment on surface albedo changes, *Atmospheric  
1203        Chemistry and Physics*, 22, 10389-10407, 10.5194/acp-22-10389-2022, 2022.
- 1204        Zhu, L., Ma, G., Zhang, Y., Wang, J., Tian, W., and Kan, X.: Accelerated decline of  
1205        snow cover in China from 1979 to 2018 observed from space, *Science of the Total  
1206        Environment*, 814, 152491, 10.1016/j.scitotenv.2021.152491, 2022.
- 1207
- 1208
- 1209